GCA-D-16-00085 Revision 3

The influence of critical zone processes on the Mg isotope budget in a tropical, highly weathered andesitic catchment

María Chapela Lara [a,*], Heather L. Buss [a], Philip A. E. Pogge von Strandmann [b], Jan A. Schuessler [c], Oliver W. Moore [a]

[a] School of Earth Sciences, University of Bristol, Wills Memorial Building, Bristol, BS8 1RJ, UK

[b] Institute of Earth and Planetary Sciences, University College London and Birkbeck, University of London, Gower Street, London, WC1E 6BT, UK

[c] GFZ German Research Centre for Geosciences, Telegrafenberg, D-14473 Potsdam, Germany

*glzmcl@my.bristol.ac.uk

ABSTRACT

In order to assess the effects of critical zone processes on Mg concentrations and isotopic signatures of tropical streams, we studied a well constrained, highly weathered andesitic volcaniclastic catchment in the Luquillo Critical Zone Observatory, Puerto Rico. Our results indicate that dissolved Mg concentrations and isotope ratios in the regolith pore water are mainly controlled by rain input, with weathering inputs being more important at sites with thinner regolith (2.7 to 0.9 m deep) and at depth (> 8 m) on a thick ridgetop regolith (~10 m). In addition to mixing of precipitation and weathering-sourced Mg, an isotopic fractionation process is taking place between dissolved Mg and the regolith, likely during dissolution or recrystallisation of Fe(III)-(hydro)oxides under alternating redox conditions. Bulk regolith is isotopically heavier than both the bedrock and the exchangeable

fraction ($\delta^{26}Mg_{regolith\ -\ bedrock}$ = + 0.03 to + 0.47‰), consistent with the preferential incorporation of heavy ^{26}Mg into secondary minerals with some exchange of sorbed Mg with isotopically lighter pore water. Magnesium concentrations in the stream show a typical dilution behaviour during a storm event, but the [Mg] − $\delta^{26}Mg$ pattern cannot be explained by mixing of rain and pore water; the data are best explained by a steady state fractionation model with α = 1.00115. During baseflow the stream has $\delta^{26}Mg$ = + 0.01‰, higher than any of the water samples or the bedrock. *In-situ* analysis of the Mg isotopic composition of bedrock minerals points at the dissolution of Mg-rich chlorite ($\delta^{26}Mg$ = + 0.19‰) as the most likely source of this isotopically heavy Mg, with mass balance calculations indicating chlorite dissolution is also the main source of Mg to the stream. Overall, our study highlights the importance of atmospheric input of nutrients to the vegetation in tropical areas covered by thick, highly leached regolith, whereas the Mg flux and Mg isotopic signature of watershed exports are dominated by bedrock dissolution delivered to the stream through deeper, usually un-sampled critical zone pathways.

Keywords: Weathering, Mg isotopes, Mg cycle, critical zone, LCZO, Puerto Rico.

1. INTRODUCTION

Magnesium is an important cation in the global silicate weathering feedback that moderates atmospheric CO_2 over geological time scales (e.g., Berner, 1995; Berner and Berner, 1997; Kump et al., 2000). In contrast to weathering proxies such as Li, which is mainly hosted in silicate minerals and is not involved in biological turnover (Tomascak et al., 2016), Mg is present in both silicate and carbonate rocks and is an essential nutrient for all life forms (Bullen, 2014; Schmitt et al., 2012). Because it is a major element in most rocks, waters, and plants, Mg is also less sensitive to the sampling and analytical issues that hamper trace element studies. Furthermore, Mg isotopes (^{24}Mg, ^{25}Mg and ^{26}Mg) are fractionated by chemical weathering (e.g., Liu et al., 2014; Pogge von Strandmann et al., 2012; Teng et al., 2010) and by the uptake by vegetation (e.g., Black et al., 2008;

Bolou-Bi et al., 2010, 2012; Tipper et al., 2010, 2012b), thus making them a promising tracer of both the geochemical and biological processes that occur in the weathering environment, which can affect the Mg isotopic composition of the streams. Consequently, a number of recent studies have examined Mg isotope ratios in the *critical zone* (see Bullen, 2014, for a recent review), defined here as the layer of terrestrial Earth extending from the bottom of the weathering zone to the top of the tree canopy. These studies have demonstrated that a range of (bio)geochemical processes can fractionate Mg isotopes, but the relative importance of these processes to Mg isotopic compositions in the critical zone is not well understood despite profound implications for understanding local and global Mg fluxes and cycles through time.

The fractionation of Mg isotopes by primary mineral dissolution has been explained experimentally by two processes: the preferential release of ^{24}Mg (e.g., Wimpenny et al., 2010) and the preferential dissolution of isotopically distinct phases (e.g., Ryu et al., 2011). However, the largest fractionations in silicate watersheds are thought to result from the incorporation of Mg into secondary minerals, with most field-based studies reporting that secondary clays are enriched in ^{26}Mg relative to their parent rock, with a $\Delta^{26}Mg_{rock-regolith}$ of + 0.5‰ to + 1.5‰ (e.g., Bolou-Bi et al., 2012; Huang et al., 2012; Liu et al., 2014; Teng et al., 2010; Tipper et al. 2012b), although Ma et al. (2015) found soils similar or slightly lighter than the shale bedrock. This fractionation is generally expressed as an enrichment in the lighter isotope, ^{24}Mg, in river waters relative to the rocks they drain (e.g., Bolou-Bi et al., 2012; Brenot et al., 2008; Pogge von Strandmann et al., 2012; Tipper at al., 2006, 2008). The mechanism of incorporation of the heavy isotope into clays is an area of active research, with field and experimental evidence suggesting that, apart from incorporation into the structure of the mineral, adsorption-desorption and ion exchange processes at mineral surfaces may also fractionate Mg isotopes in weathering, with the direction and extent of this fractionation still a matter of debate (Bolou-Bi et al., 2012; Huang et al., 2012; Jacobson et al., 2010; Li et al., 2014; Opfergelt et al., 2012, 2014; Pogge von Strandmann et al., 2012; Tipper et al., 2010, 2012a; Wimpenny et al., 2015).

The isotopic effects of Mg sorption onto secondary minerals other than clays, such as oxides and hydroxides, are essentially unknown, with no direct measurements published to date.

Nevertheless, several studies have found that sorption onto Al- or Fe-(hydr)oxides in both experimental and natural environments can isotopically fractionate other divalent metals (Cu, Zn, Fe) with a preference for the heavy isotope (e.g., Balistrieri et al., 2008; Pokrovsky et al., 2005; Mikutta et al., 2009). This fractionation can occur even at low pH for Fe(III)-hydroxides (e.g., Violante et al., 2002), indicating Mg isotope fractionation by sorption-desorption into Al-or Fe-(hydr)oxides is possible in highly weathered regoliths, as interpreted by Liu et al. (2014) for the enrichment in ^{26}Mg in bauxites relative to the bedrock.

Fractionation of Mg isotopes by vegetation uptake has been demonstrated in laboratory (Black et al., 2008; Bolou-Bi et al., 2010) and field studies (Bolou-Bi et al., 2012; Tipper et al., 2010, 2012b; Opfergelt et al., 2014), with a general enrichment in ^{26}Mg in plants relative to pore waters or nutrient solutions. There is also a fractionation within the plant associated with the translocation of Mg from roots to leaves, and with foliage age (Bolou-Bi et al., 2010, 2012). The effect of vegetation uptake has been regarded as a factor controlling the Mg isotopic composition of streams (Bolou-Bi et al., 2010, 2012; Tipper et al., 2012b; Opfergelt et al., 2014), although less important than reactive transport during water-rock or water-soil exchange complex interactions (Bolou-Bi et al., 2012; Tipper et al., 2012b; Opfergelt et al., 2014), which in turn depend on the sources of Mg, the flow paths and the flow rates of water through the critical zone, and on the rates of Mg isotope fractionation, which can only be known at the catchment scale.

The vast majority of field-based studies of Mg isotopes has been focussed on temperate and arctic sites, in spite of the fact that the tropics are disproportionately more important, relative to their land area, in terms of weathering inputs to the oceans, biodiversity and climate change sensitivity (e.g., Chapin et al., 2010; Stallard and Edmond, 1983; Wohl et al., 2012). Equally, Mg isotope systematics during critical zone processes in temperate watersheds cannot be directly extrapolated to the tropics, which are different in a number of ways. One key difference is that the Mg isotope ratios of streams are strongly influenced by seasonality in temperate regions, expressing changes in critical zone processes such as vegetation uptake and water-rock interaction time (e.g., Bolou-Bi et al., 2012; Tipper et al., 2012b), whereas tropical, high precipitation sites have significantly less seasonality. The

92 hydrological functioning of tropical high precipitation catchments also has important peculiarities
93 related to the thick, clay-rich saprolite that often mantles these environments, leading water to flow
94 laterally along high-permeability, near-surface flow paths or via saturation-excess overland flow
95 during intense rain events (Elsenbeer, 2001; Schellekens et al., 2004; Goller et al., 2005; Bonell,
96 2005; Kurtz et al., 2011). Finally, recent studies on the Caribbean island of Guadeloupe have found
97 that atmospheric inputs can have a strong influence on the δ^{26}Mg of bulk soil (Dessert et al., 2015)
98 and the exchangeable fraction (Opfergelt et al., 2012) of cation-depleted tropical regoliths.

99 Aiming to fill the gap in Mg isotopic data from the tropics and to generally improve our
100 understanding of the Mg cycle in the critical zone, here we examine the controls on the Mg dynamics,
101 at several temporal and spatial scales, in a well-constrained tropical catchment in the Luquillo Critical
102 Zone Observatory (LCZO), Puerto Rico (Fig. 1). Specifically, we seek to distinguish the biological
103 from the geochemical components of the Mg cycle and to quantify their relative contributions to the
104 Mg solute fluxes in the watershed. We hypothesize that the largest input to the whole critical zone Mg
105 budget is the dissolution of bedrock minerals, and that dissolution-precipitation during weathering
106 controls the δ^{26}Mg of the deep critical zone over all the time scales studied. In the regolith, we
107 hypothesize that Mg fluxes and δ^{26}Mg values over short time scales (days to decades) are strongly
108 affected by cycling by vegetation within the rooting zone, but are more influenced by dissolution of
109 atmospheric dust over intermediate time scales (decades to kyears). In the stream, we expect the
110 δ^{26}Mg signature to reflect rain and shallow pore water during storm events and deeper critical zone
111 sources during baseflow.

112 To test these hypotheses, we measured the Mg concentrations and Mg isotopic ratios of
113 precipitation; stream water during baseflow and storm flow; bedrock; vegetation; and depth profiles
114 of pore water (at different topographic positions), bulk regolith and exchangeable Mg. We compare
115 the relative influence of different Mg sources, fractionation processes and time scales on the Mg
116 isotope signature of stream water at baseflow and storm flow.
117

2. FIELD SETTING

Environmental data has been gathered in the Luquillo Mountains of north-eastern Puerto Rico for more than 20 years by the US Forest Service International Institute of Tropical Forestry (IITF), the US Geological Survey's Water Energy and Biogeochemical Budgets (WEBB) project, and the NSF Long Term Ecological Research (LTER) program. Building on this history, the NSF Luquillo Critical Zone Observatory (LCZO) was founded in 2006. The LCZO, therefore, provides one of the best instrumented and contextualised sites in the world in which to study tropical critical zone processes. For this study, we focus on a small volcaniclastic catchment (Bisley 1) that is part of the Rio Mameyes watershed that drains north into the Atlantic Ocean (Fig. 1). This catchment is underlain by Cretaceous, marine-deposited, quartz-poor meta-volcaniclastic rocks of the Fajardo Formation (Jolly et al., 1998), which is dominated by thick-bedded tuff breccias with andesitic clasts, interbedded with coarse-grained tuff, tuffaceous sandstone and cherty siltstone (Briggs, 1973). The bedrock was altered during diagenesis and hydrothermal metamorphism, during which the fine-grained groundmass was devitrified, sericitized and chloritized; phenocrysts of biotite, plagioclase and augite were replaced by chlorite and actinolite (Buss et al., 2013; Table 1).

The warm and humid climate of the Luquillo Mountains (Table 1) has favoured intense and rapid weathering (e.g., White et al., 1998; Dosseto et al., 2012), producing a mantle of regolith that can reach at least 37 m deep in the Bisley 1 catchment (Buss et al., 2013). Here we define all the weathered material developed over the bedrock as regolith (including saprolite and soil). The primary minerals of the volcaniclastic bedrock weather mostly *in situ* to microcrystalline disordered kaolinite and halloysite, illite, and Fe- and Al-oxides (Buss et al., 2017; Dosseto et al., 2012; Huffaker, 2002; Porder et al., 2015; Table 1). Occasional accumulations of Mn-oxides are visible in the saprolite as mm-thick layers. The deepest regolith also contains about 7 – 12 wt% chlorite and 2 – 4 wt% feldspars (Tables 1 and S3; Buss and White, 2012; Buss et al., 2017), consistent with an approach to parent rock composition at depth. This saprolite produces clay-rich but moderately well-drained ultisols (Scatena, 1989; Johnston, 1992) that are mantled by a thin layer of leaf litter in most areas.

We focused our work on a regolith depth profile from a ridgetop site (B1S1 in Fig. 1), classified as a Typic Haplohumult (Yi-Balan et al., 2014; Huffaker, 2002), for which major element chemistry, mineralogy, microbiology and physical properties have been presented in Buss et al. (2017) and Liermann et al. (2014). This regolith is highly leached, containing only secondary minerals and quartz above 8 m depth (Liermann et al., 2014) and, in contrast to the usual trends with depth (e.g., Brantley and Lebedeva, 2011), many parameters show a discontinuity at ~1 m depth. For instance, bulk density is expected to increase steadily with depth (Brady and Weil, 2007), but here it increases from 0.9 m to 1.5 m depth (Buss et al., 2017). Similarly, water contents are high throughout the profile (35 to 25 vol.%), but the minimum is reached from 0.9 m to 1.5 m depth (Buss et al., 2017). The regolith is moderately to strongly acidic at all depths (average pH =3.6; Liermann et al., 2014). A full soil pit description by horizon at this site can be found in Yi-Balan et al. (2014), who report two layers with redoximorphic features (mottling, red and gley layers) indicative of alternating redox conditions, most marked between 1.0 and 1.4 m depth.

3. METHODS

3.1 Sample collection

We obtained splits of regolith from four cores augered during the installation of pore water samplers along a slope transect (Figs. 1, 4; Buss et al., 2017), from the top of a ridge (B1S1) to the riparian zone of Bisley 1 stream (B1S4, Figs. 1, 4), and from two bedrock cores drilled on the nearby road (Fig. 1; Buss et al., 2013). We selected a thin section from one of these cores for analysis of the Mg isotopic composition of individual minerals in the bedrock (sample B1W2 at 6.4 m depth in Buss et al., 2013; Table S1).

To investigate the Mg cycle at different time scales we analysed the Mg isotopic composition of the regolith at the ridgetop site in three different reservoirs. 1) Pore water, which reflects processes at the scale of water residence time in the regolith (~2 years, Buss et al., 2017); 2) the exchangeable fraction (NH_4-acetate extract, method in Buss et al., 2017), reflecting Mg sorbed onto minerals and

171 approximating longer-term bioavailability; and 3) the bulk solid, reflecting processes over the time
172 scale of regolith development (~30 ky; Dosseto et al., 2012).

173 The temporal variability of Mg concentrations in pore water, sampled from suction lysimeters,
174 is discussed in Buss et al. (2017). We sampled lysimeters for Mg isotope analysis in November 2009.
175 Samples were filtered to 0.45 µm (SFCA-membrane, Cole-Parmer) into acid-washed HDPE bottles
176 following procedures used by the USGS at this site (e.g., Murphy and Stallard, 2012). Preliminary Mg
177 isotope analyses were conducted at the *Institute de Physique du Globe de Paris* on pore waters
178 collected from three of the four sites in January 2008 (Chapela Lara et al., 2014), and are presented
179 here for comparison.

180 Stream water samples were collected during a storm event in June 2011 at the gaged outlet of
181 the catchment; major and some trace elements were analysed by ICP-AES. Openfall precipitation was
182 collected above the canopy at the head of the catchment (Fig. 1). To calculate Mg fluxes at the
183 catchment level we used the LTER online database for daily stream discharge from 2000 to 2005,
184 daily rain discharge from 2000 to 2011 (Gonzalez, 2011a,b), and weekly chemical composition of the
185 stream and precipitation from 2000 to 2010 (McDowell, 2010, 2012).

186 Plant leaves and bark samples were collected at the ridgetop site (B1S1) by the USGS, oven
187 dried and powdered. Here we present only the results of the bark of the predominant species,
188 Tabonuco tree (*Dacryodes excelsa*), which accounts for 45.7% of the aboveground biomass in this
189 catchment (Scatena et al., 1993).
190

191 **3.2 Elemental and isotopic analysis**
192

193 The elemental composition of the plant samples was measured by ICP-OES at the Central Analytical
194 Laboratory in the Department of Crop and Soil Science, Oregon State University. Major and trace
195 elements in pore water, bulk regolith, ammonium acetate extractable cations, and bedrock samples
196 were analysed by the USGS by ICP-MS after multi-acid digestion, or by SGS Laboratories (Toronto,
197 Ontario, Canada) by ICP-AES after lithium metaborate fusion digestion; much of this data was

198 presented in Buss et al. (2013, 2017) but Nb data and additional samples are presented here (Table
199 S1). Splits of those samples (plant, regolith and bedrock samples) and rock standards were digested in
200 an ultra-pure concentrated acid mixture (HF, HCl, HNO_3) for Mg isotope analysis.

201 We purified all samples using the cation exchange chemistry procedure detailed in Pogge von
202 Strandmann et al. (2011). Briefly, an amount of sample containing ~1 µg Mg was dried, treated with
203 HNO_3+H_2O_2 to remove any organic matter, re-dissolved in 2M HNO_3, and passed through two sets of
204 chromatographic columns filled with Biorad AG50W X12 cation exchange resin. Because of high
205 Ti/Mg ratios, bulk regolith samples underwent an additional purification step to remove Ti, whose
206 ions cause interferences when measuring Mg isotopes in low-resolution mode of the MC-ICP-MS.
207 For this, we used an additional set of columns with 0.25 mL of TRU-Spec resin and 7M HNO_3 as the
208 eluent (Pogge von Strandmann et al., 2012). We measured the Mg isotope ratios on a Thermo
209 Neptune multi-collector ICP-MS at the Bristol Isotope Group laboratory, using the standard-sample
210 bracketing technique (DSM-3 standard), with a concentration within ± 10% of that of the sample.
211 Results were normalized using the common delta notation in per mil (Galy et al., 2003):

212 $$\delta^{x}Mg\ (‰) = \left(\frac{\left[\frac{^{x}Mg}{^{24}Mg}\right]_{sample}}{\left[\frac{^{x}Mg}{^{24}Mg}\right]_{standard}} - 1 \right) \times 1000 \quad (1)$$

213 where x can be 25 or 26. We monitored the long-term precision of our measurements with the Mg
214 Cambridge-1 standard (CAM-1), which yielded δ^{26}Mg = –2.56 ± 0.10 ‰ (2sd, n = 54) over a period
215 of two years, and our pore water sample B1S1 (δ^{26}Mg = – 0.77 ± 0.04 ‰, 2sd, n = 14). The accuracy
216 and precision of our whole chemical and analytical procedure were assessed by repeated measurement
217 of seawater and USGS rock standards BHVO-2 and BCR-2 (Table 2). The average δ^{26}Mg of seawater
218 (– 0.85 ± 0.07 ‰, n = 13) is within analytical uncertainty of the values measured by Ling et al. (2011)
219 and Foster et al. (2010), and its 2sd is used as the external reproducibility.

220 The Mg-bearing minerals (pyroxene, amphibole and chlorite) in the thin section selected for *in*
221 *situ* Mg isotope analyses (B1W2-2-2) were identified and quantified by elemental mapping using
222 EDX analysis (Thermo 10 mm^2 silicon drift detector), coupled with backscatter electron (BSE)

imaging on a scanning electron microscope (SEM, Hitachi S-3500N) at the University of Bristol. The elemental compositions of these minerals were then determined using WDS electron probe microanalysis (EPMA, Cameca SX100; Table S2).

The micro-scale Mg isotope composition of individual minerals and their Mg and Al concentrations were determined by UV femtosecond laser ablation coupled to a Thermo Neptune MC-ICP-MS (fsLA-MC-ICP-MS, *Fem2*) in the Helmholtz Laboratory for the Geochemistry of the Earth Surface at GFZ Potsdam. Instrumentation, data acquisition and evaluation procedures are detailed in Schuessler and von Blanckenburg (2014). Laser ablation was performed on individual mineral grains with a spatial resolution of less than 100 x 100 µm surface area, with less than 10 µm crater depth. The laser beam, with a diameter of ~25 µm, was scanned across the mineral surface to adapt to the irregular shape of the grains with repetition rates between 20 to 40 Hz. The high mass resolution mode of the MC-ICP-MS was used for Mg isotope ratios measurements, which is capable of resolving isobaric interferences during laser ablation ($^{52}Cr^{2+}$ on $^{26}Mg^{+}$, $^{50}Ti^{2+}$ and $^{50}Cr^{2+}$ on $^{25}Mg^{+}$, or $^{48}Ca^{2+}$ and $^{48}Ti^{2+}$ on $^{24}Mg^{+}$; Oeser et al., 2014). Mass bias correction was performed using the komatiite glass GOR132-G as bracketing standard. We converted our results to δ-values relative to DSM-3 using a $\delta^{26}Mg$ value for GOR132-G of − 0.17 ‰ relative to DSM-3 (Oeser et al., 2014; Tables 3, S5). Silicon was used as an internal standard element (*IS*, determined independently) for determination of Mg and Al concentrations with an uncertainty estimated to be better than 5% (Table S1).

At the current level of experience in the novel fsLA-MC-ICP-MS method for Mg isotope ratios measurement, we report a rather conservative estimate of uncertainty of ± 0.12‰ (2sd) for $\delta^{25}Mg$ and ± 0.25‰ (2sd) for $\delta^{26}Mg$, which are nevertheless sufficient to interpret the measured mineral $\delta^{26}Mg$ data within the scope of this study. This uncertainty is based on repeated measurements on reference materials during four analytical sessions (Table S3) and encompasses differences in the analyses induced by day to day instrument performance and tuning (Fig. S1). The measurements of BHVO-2G basaltic glass (average $\delta^{26}Mg$ = − 0.17 ± 0.25‰, 2sd, n = 26) agree within uncertainty with published values from bulk rock analyses and the recommended value for this reference material (− 0.20 ±

0.07‰; Teng et al., 2015; Fig. S1, Table S3). To evaluate differences in δ^{26}Mg between mineral phases in the rock sample, we also computed the student-t corrected 95% confidence intervals of the mean values from repeated individual laser ablation measurements on multiple grains (Fig. 8, Table 3). Moreover, we validated the method on the specific chemical matrix composition of the investigated samples in this study. For this purpose glasses made from bulk sample powders B1W2-2-2 and B1W2-6-2 (Table 2) by flux free fusion using an Ir strip heater (Stoll et al., 2008) were measured using fsLA-MC-ICP-MS. The obtained Mg isotope values are in good agreement with the bulk Mg isotope values of the same sample powders analysed by solution MC-ICP-MS after acid-digestion and Mg column chemistry purification (Table 3, Fig. 8).

4. RESULTS

4.1 Mg loss and degree of weathering of the regolith

Most cations are lost from the regolith between 1 m and 8 m depth (Buss et al., 2017), including Mg (Fig. 2c). The cation exchange capacity (estimated from the total NH_4-acetate extractable cations) of this regolith is very low (Buss et al., 2017), from 0.5 $cmol_c\ kg^{-1}$ at 0.6 m depth to a maximum of 2.7 $cmol_c\ kg^{-1}$ at the deepest sample. Similarly, Mg contents are also low, from 1.47 to 10.1 $mmol\ kg^{-1}$ (Fig. 2b), constituting only between 1% and 5% of the bulk Mg. Dissolved Mg in pore water is even lower and does not show a clear trend with depth (Fig. 2a), in contrast to the longer-term pools that increase progressively with depth below 1.2 m depth (Figs. 2b,c).

To estimate the fraction of Mg remaining in the regolith after weathering has proceeded (f_{Mg}), we used the average composition of the bedrock samples (Table S1) as the starting parent material, and we chose Nb as the index element because it is comparatively immobile in tropical settings (e.g., Kurtz et al., 2000; Ma et al., 2007). The results describe a Mg-poor regolith characterised by a depletion profile from 9.7 m to 1.2 m depth (f_{Mg} from 0.14 to 0.01), that becomes slightly more enriched in Mg above 1.2 m depth (f_{Mg} = 0.1 at the surface, Fig. 3a).

To measure the overall degree of alteration of the regolith we used the Parker Index of Weathering (WIP), regarded as the most appropriate alteration index for heterogeneous parent rocks and highly weathered regolith, because it includes only the most mobile oxides and allows for Al mobility. This index is calculated from molar concentration proportions as (Price and Velbel, 2003):

$$\mathrm{WIP} = 100 \cdot \left[\frac{2Na_2O}{0.35} + \frac{MgO}{0.9} + \frac{2K_2O}{0.25} + \frac{CaO}{0.7}\right] \quad (2)$$

where a fresh rock can have WIP >100 and a totally weathered sample would have WIP = 0. The regolith at the ridgetop site (B1S1) is the most weathered of the four; the two located on slopes (B1S2 and B1S3) achieve similar alteration to the ridgetop site, but over much less depth (Fig. 3b). The thinnest profile, at the riparian site (B1S4), is the least altered at depth and has the largest variation in WIP, going from values typical of fresh rock (~300) to a WIP of 37 over less than a meter of depth (Fig. 3b).

4.2 Mg and δ^{26}Mg of water and vegetation

Magnesium concentrations, [Mg], in openfall ranged between 2 and 150 µM L^{-1} from 2000 to 2010 (Table S4). Mg in pore water ranged between 4.9 µM to 37.3 µM L^{-1} during 2008, with the highest values in the valley site B1S4 (Table S5; Buss et al., 2017). Magnesium concentration in pore water is most variable in surficial samples (varying by up to 9.7 µM L^{-1} on the ridgetop site), and comparatively stable below 4 m depth (Fig. 4). This variation does not otherwise follow a clear pattern with depth but, on average, the lowest values are in the uppermost samples and the highest below 4 m depth (Fig. 4; Buss et al., 2017). Compared with the longer-term pools represented by the exchangeable fraction and the bulk regolith, Mg is the most variable in the short-term pool represented by pore water (Fig. 2a).

The Mg isotope composition of all samples is summarised in Fig. S1 and Table 2. The measured δ^{26}Mg values of local openfall precipitation (– 1.10‰ to – 0.92‰) are within uncertainty or slightly lower than seawater δ^{26}Mg (– 0.85 ± 0.07‰). Tabonuco bark (the dominant species in this ecosystem), has δ^{26}Mg = – 0.72‰, within the range of published vegetation values but lighter than

most plants collected in the field (Schmitt et al., 2012, and references therein). Pore water δ^{26}Mg in the ridgetop profile (B1S1) shows a clear trend with depth (r = 0.96), increasing from – 0.78‰ at the surface (0.15 m) to – 0.22‰ at 9.3 m depth (Fig. 5). Within this trend there is a heavy excursion from 0.6 to 1.2 m depth, with δ^{26}Mg reaching a local maximum of – 0.67‰ at 0.9 m depth (Table 2, Fig. 5). A similar pattern is apparent in the other profiles along the slope transect, and three of them also record a heavy excursion in δ^{26}Mg at ~ 1 m depth (Fig. 6). These features are present in samples collected both in 2008 and in 2009 (Chapela Lara et al., 2014; shown for the ridgetop site in Fig. 6). The valley site has higher [Mg] and δ^{26}Mg than the other sites (e.g., B1S1 δ^{26}Mg = – 0.78‰, B1S4 = – 0.59‰), consistent with its lower degree of weathering (Fig. 3b).

Magnesium concentrations in the stream during the storm event varied between 10.6 µM L^{-1} and 45.7 µM L^{-1}, similar to values reported by Schellekens et al. (2004) in the neighbouring Bisley 2 catchment during storm flow and baseflow, respectively. The δ^{26}Mg values ranged from + 0.01‰ to – 0.74‰, lower than the bedrock and the bulk regolith except for the end of the event when the stream returned to a low-level stage (Fig. 7). Mg isotope ratios and [Mg] in the stream samples are linearly correlated (r^2 = 0.98), with the highest [Mg] and heaviest δ^{26}Mg values (+ 0.01‰) during baseflow and the lowest [Mg] and lightest δ^{26}Mg (– 0.74‰) during high stage (Fig. 7).

4.3 Mg isotopic composition of the bulk regolith and the exchangeable fraction

The δ^{26}Mg values of bulk regolith in the ridgetop site show a gradual enrichment in the heavy isotope as weathering proceeds, from values close to the bedrock at the deepest sample (δ^{26}Mg = – 0.07‰, Fig. 5) to a maximum of + 0.37‰ at 1.8 m depth (Fig. 5); from 1.8 m to the shallowest sample (0.6 m depth) δ^{26}Mg decreases. The δ^{26}Mg of the exchangeable fraction of the regolith is the least variable of the three pools studied (pore water, exchangeable, bulk), with similar values to the bedrock from 9.3 m up to 6 m depth. However it does show a decreasing δ^{26}Mg trend above 3 m depth, reaching δ^{26}Mg = – 0.47‰ at the shallowest sample (0.6 m, Fig. 5). The difference in δ^{26}Mg between the three pools studied increases towards the surface of the profile (Fig. 5). For example, the measured $\delta^{26}Mg_{regolith -}$

330 $_{pw}$ is + 0.72‰ on average, but as low as + 0.15‰ at 9.7 m depth and as high as + 1.09‰ at 0.6 m
331 depth. Pore water and the exchangeable fraction have similar δ^{26}Mg values ($\Delta^{26}Mg_{exch-pw}$ from +
332 0.07‰ to + 0.37‰, Fig. 5).

333
334 **4.4 Mg isotopic composition of the bedrock**
335
336 The Mg isotope composition of the andesitic unweathered bedrock (– 0.17‰ to – 0.05‰) is within
337 the range of published values for intermediate igneous rocks (Dessert et al., 2015; Teng et al., 2015).
338 Mg-rich chlorite, the most abundant Mg-bearing phase in the bedrock (20.4 wt%, Buss et al., 2013),
339 has an average δ^{26}Mg of +0.19 ± 0.08‰ (2SE$_t$, n=9) as determined by laser ablation MC-ICP-MS
340 (Fig. 8, Table 3). This is considerably heavier than the value published by Ryu et al. (2011) from
341 mineral separates of granite (– 1.82 ± 0.07‰), or by Pogge von Strandmann et al. (2015) from
342 metamorphic chlorite at the slab-mantle interface (– 1.03 to + 0.02‰), although lighter samples from
343 that study were altered by diffusion. The other Mg-bearing phases present in the rock, pyroxene and
344 amphibole, have average δ^{26}Mg values of – 0.16 ± 0.15‰ and – 0.33 ± 0.44‰, respectively (Fig. 8,
345 Table 3), similar to published values for mineral separates of Fe-Mg silicates measured after
346 dissolution (hornblende = – 0.32 to –0.14‰, Liu et al., 2010, and Ryu et al., 2011; biotite = – 0.40 to
347 + 0.44‰, Liu et al., 2010, Ryu et al., 2011, and Shen et al., 2009; olivine = – 0.27 ± 0.07‰, Teng et
348 al., 2015).

349 Using the abundances and Mg concentrations of chlorite (Buss et al., 2013), pyroxene and
350 amphibole (Table S2), which are the three significant Mg-bearing minerals in the rock, together with
351 their Mg isotope compositions (Table 3), we calculated a bulk rock [Mg] of 4.41 wt.% and an average
352 δ^{26}Mg of – 0.05‰, in reasonable agreement with the average measured values for the bulk bedrock
353 (3.30 wt% Mg, Buss et al., 2013; δ^{26}Mg = – 0.10‰, this work).

354

355 **5. DISCUSSION**

5.1 Controls on the Mg and δ^{26}Mg of pore waters

5.1.1 Atmospheric inputs

To estimate the contribution of rain to pore water [Mg] we applied the common chlorine balance method to the ridgetop site (White et al., 2009; Buss et al., 2017), where we can assume vertical 1D water flow. We used the average [Mg] and [Cl] of pore water (Table S4), and the average [Mg] and [Cl] in openfall from 2006 to 2008. We estimate that rain-sourced Mg constitutes between 71% and 93% of total Mg in pore water, resulting in very low rain-corrected Mg concentrations (1.1 to 7.7 µM L^{-1}, Fig. 4). The maximum rain input is reached at 1.2 m depth and not in the most surficial samples as we expected. Furthermore, Mg concentrations (either raw or rain-corrected) do not show a clear trend with depth (Fig. 4), as opposed to the expected pattern of predominance of rain at the surface and a gradual increase of weathering inputs towards the base of the profile; no concentrating effect of evapotranspiration is apparent at the surface of the profile either.

In contrast to Mg concentrations, δ^{26}Mg values do show a clear trend with depth (r = + 0.96), with values close to those of rain near the surface and heavier values, close to those of bedrock, at depth (Fig. 5), as has been reported in regolith pore water at other sites (Bolou-Bi et al., 2012; Tipper et al., 2010). However, our pore water data do not plot along a straight line in δ^{26}Mg vs. 1/Mg space (not shown) as would be expected for a two end-member mixing, indicating that a fractionation process is likely contributing to the Mg isotopic ratios of this profile, which is further discussed in Section 5.1.3. The heavy excursion at ~ 1 m depth cannot be explained by a difference in rain inputs either: at this depth samples have the highest rain inputs (Fig. 4), which would shift δ^{26}Mg towards rain-like values (– 0.97‰), the opposite of what we observe (Fig. 5).

Another source of atmospheric Mg input to the catchment could be Saharan dust, which has been found to be a significant source of nutrients to the Luquillo Mountains (e.g., Pett-Ridge, 2009; Pett-Ridge et al., 2009). However, Stallard (2001) did not observe a significant contribution of Mg in the desert-dust component of a 13 year study of precipitation at El Verde (8.2 km from our study site), consistent with our data not showing an enrichment in Mg in pore water near the surface of the

regolith (Figs. 2a, 4). The ultimate reason for the lack of dust-derived Mg in rain and pore water may be the fact that Saharan dust reaching Puerto Rico is composed of relatively insoluble secondary clays (more than 85% illite, kaolinite and montmorillonite; Reid et al., 2003), which are most likely to contribute to the Mg solid load rather than the dissolved load of the catchment as has been observed on the Caribbean island of Bermuda (Herwitz et al., 1996). Indeed, there is an enrichment of Mg in bulk regolith above 1.5 m depth (Figs. 2c, 3a) paired with a shift in δ^{26}Mg towards silicate-like values (Fig. 5), whereas such features are not apparent in the most surficial pore water samples (Fig. 5). Atmospheric inputs to the bulk regolith are also evidenced by a small increase in the chemical alteration index above 1.2 m depth (Fig. 3b, Table S1), a feature that was also reported by Dosseto et al. (2012) at another ridgetop profile in this catchment.

5.1.2 Vegetation uptake

Because the soil at this site is strongly depleted in Mg and tropical vegetation tends to operate tight nutrient cycles close to the surface (Jordan and Herrera, 1981; Vitousek, 1984; Wood et al., 2009), we expected to find a strong fractionation effect of vegetation uptake over surficial pore water δ^{26}Mg. On the contrary, pore water samples within the rooting zone (0.0 to 0.6 m depth) have δ^{26}Mg similar to rain (within the uncertainty of ±0.07‰), with $\Delta^{26}Mg_{pw-rain}$ of + 0.20‰ on average (Figs. 5, S2). This difference is lower than previously published studies, that commonly show an effect of vegetation uptake of around + 0.25‰ (e.g., Black et al., 2008; Bolou-Bi et al., 2010, 2012; Tipper et al., 2010, 2012b), but that can be as high as + 1.05‰ (Bolou-Bi et al., 2010). The Tabonuco tree sample has δ^{26}Mg = − 0.72‰, very similar to the surface pore water value of − 0.77‰, but we recognise that the largest Mg isotope fractionation is expected to occur at the root level (Bolou-Bi et al., 2010), which we did not analyse, and during intra-plant translocation (Black et al., 2008; Bolou-Bi et al., 2010, 2012). Therefore, although the small differences in δ^{26}Mg between pore water, rain and vegetation suggest the effect of plant uptake on the isotopic composition of the soil over pore water residence times is likely to be minor, more extensive vegetation analyses are clearly required.

410

411 **5.1.3 Geochemical mechanisms of Mg isotope fractionation in the regolith**

412

413 In Section 5.1.1 we found that rain is the main source of Mg to pore water (Fig. 4), with input from
414 bedrock dissolution to the deepest samples (Figs. 5, 6), but that in addition to mixing between these
415 two components a fractionation mechanism is also necessary to explain the observed δ^{26}Mg – [Mg]
416 pattern. Because the effect of vegetation uptake on pore water δ^{26}Mg is of subordinate importance
417 below the rooting zone (0.6 m), this fractionation is likely due to geochemical reactions within the
418 regolith. With the exception of minor illite (most of which is secondary), there are no primary Mg-
419 containing minerals left above 8 m depth in the regolith profile (Table S3; Buss et al., 2017), which
420 limit the plausible geochemical fractionation processes to *i)* the precipitation or dissolution of
421 secondary minerals, *ii)* the sorption or desorption of Mg onto/from secondary minerals (clays,
422 gibbsite, goethite, or other (hydr)oxides of Fe, Mn or Al), and *iii)* microbial activity.

423 The higher δ^{26}Mg of bulk regolith relative to the bedrock and pore water (Fig. 5, S2) is
424 consistent with secondary minerals preferentially incorporating the heavier ^{26}Mg isotope, in
425 agreement with most studies of δ^{26}Mg in the weathering environment (e.g., Bolou-Bi et al., 2012;
426 Huang et al., 2012; Liu et al., 2014; Teng et al., 2010; Tipper et al., 2010). Furthermore, the lower
427 δ^{26}Mg of the exchangeable fraction relative to the bulk regolith (Figs. 5, S2) is in agreement with
428 recent experimental results that indicate that exchangeable Mg adsorbed into interlayer spaces and
429 charged surface sites is relatively enriched in light ^{24}Mg compared to the residual structural Mg in
430 clay (Wimpenny et al., 2014). Nonetheless, the mineralogy of the regolith is dominated by kaolinite
431 and other 1:1 clays (Table 1, S3), which can hold little Mg within its mineral lattice or at
432 exchangeable sites, and we do not find a correlation between clay contents and δ^{26}Mg in any of the
433 regolith pools studied.

434 The bulk regolith δ^{26}Mg approximately increases as the contents of Fe(III)-(hydr)oxides also
435 increase ($r = + 0.62$; Fig. 9a) and δ^{26}Mg in the exchangeable fraction decreases ($r = - 0.70$; Fig. 9b).

These opposite trends suggest that the isotopically heavy Mg may be preferentially bound within the Fe(III) – (hydr)oxide grains, while isotopically light Mg forms readily exchangeable surface complexes. Thus when Fe(III)-(hydr)oxides dissolve during periods of reducing conditions (Liptzin and Silver, 2009), they would preferentially release ^{26}Mg into the pore water. This explanation is supported by the coincidence in space of redoximorphic features indicative of temporarily reducing conditions (1.0 to 1.4 m depth; Yi-Balan et al., 2014), an increase in ferrous iron (Liermann et al., 2014), and the heavy excursion in pore water δ^{26}Mg at ~1 m depth.

Another explanation for our observations can be that the Fe from soils in this catchment is composed predominately of short-range-order Fe phases (Peretyazhko and Sposito, 2005), which are subjected to extensive atom exchange and recrystallisation processes (Tishchenko et al., 2015). These 'ripening' processes are known to expel trace metals from co-precipitated iron phases (e.g., Pedersen et al., 2005; Frierdich and Catalano, 2012) and could be expelling Mg to the more labile surface complexes as crystallinity increases, as suggested by an increase in exchangeable Mg as total Fe increases ($r = + 0.60$; Fig. 9c) and crystalline Fe(III)–(hydr)oxides decrease ($r = – 0.72$; Fig. 9d). This combined process would preferentially release the heavy isotope, as suggested by the inverse correlation between Fe(III)–(hydr)oxides and δ^{26}Mg in the exchangeable fraction (Fig. 9b). This process could also account for the heavy excursion in pore water δ^{26}Mg at ~ 1 m depth, because oscillating redox conditions have been shown to enhance the crystallisation of Fe(III)-(hydr)oxides phases (Thompson et al., 2006).

Microbial metabolism might be yet another mechanism for Mg isotope fractionation within the regolith, as Mg is the most common divalent metal in living cells (e.g., Fagerbakke et al., 1999; Heldal et al., 2012). The fractionation of Mg isotopes by microbial activity has been demonstrated for forsterite dissolution (Oelkers et al., 2015), although other studies report negligible fractionation during Mg uptake by cyanobacteria (Mavromatis et al., 2012). In our regolith the abundance of microbial cells (Liermann et al., 2014) is correlated with δ^{26}Mg in pore water ($r = – 0.70$; Fig. 9f), suggesting bacteria might be preferentially taking up the heavy isotope. If this were the case, we can

speculate that the fluctuating redox conditions from 1.0 to 1.4 m depth may cause periodic die-offs of microbial populations, releasing heavy ^{26}Mg into the pore water, which is consistent with a sharp decrease in cell numbers at 1.1 m depth (Liermann et al., 2014) and with the heavy anomaly in pore water $\delta^{26}Mg$ (Fig. 5).

5.2 Controls on the Mg and $\delta^{26}Mg$ of the stream

5.2.1 Mixing, fractionation and the source of baseflow Mg

Magnesium in the stream shows a typical dilution behavior, with the highest concentration during baseflow, becoming progressively lower as the storm proceeds. Mg isotope ratios seem to follow a similar dilution trend, with the heaviest values during baseflow (Fig. 7), so we expected the Mg isotopic composition of the stream to reflect mixing between baseflow Mg sources (deep pore water, groundwater) and stormwater sources (direct rainfall, runoff, and shallow pore water). However, Mg concentration and $\delta^{26}Mg$ in the stream are strongly, linearly correlated ($r^2 = 0.98$) during the entire storm event (Figs. 10, 11), not following the expected pattern of binary mixing that would produce a hyperbola in a $\delta^{26}Mg$ vs. Mg space (Langmuir et al., 1987). Likewise, there is a good correlation between $\delta^{26}Mg$ and ln[Mg] ($r^2 = 0.92$, not shown). These clear $\delta^{26}Mg$ – Mg trends suggest that, although dilution by storm sources may be controlling the stream [Mg] during the storm event, it is isotopic fractionation that is driving the $\delta^{26}Mg$ signature, in agreement with previous works that show fractionation due to weathering-related processes is the predominant factor controlling $\delta^{26}Mg$ in small rivers (Tipper et al., 2006, 2008).

Apart from following a linear trend in a $\delta^{26}Mg$ vs. Mg space, to account for the observed data any fractionation processes (± mixing with storm water sources) must fulfil two conditions: *i)* start from an initial reservoir with an isotopic composition that is at least as enriched in ^{26}Mg as the baseflow ($\delta^{26}Mg = + 0.01‰$), and *ii)* be capable of modifying the stream $\delta^{26}Mg$ - Mg at the time scale of the duration of the storm event (~ 6 h; Fig. 5).

488

489 ***Baseflow source***
490

491 Our findings support a source of water to the stream deeper than any of the sampled pore waters,
492 which have a maximum δ^{26}Mg value of − 0.22‰ (Table 2; Figs. 6, S2). This implies that there are
493 sources other than rain and pore water contributing to the Mg budget of the stream, in agreement with
494 indirect evidence from previous studies at the Bisley catchments using S isotopes (Yi-Balan et al.,
495 2014) and elemental chemistry (Schellekens et al., 2004). Among our sampled Mg-bearing reservoirs
496 only chlorite (Fig. 8) or the bulk regolith above 8.2 m depth (Fig. 5) have the necessary heavy Mg
497 isotope composition, but the dissolution rate of silicates, in the order of 10^{-14} to 10^{-16} mol m^{-2} s^{-1} (e.g.,
498 Buss et al., 2017; White and Buss, 2013), would make them irrelevant for a short storm event.
499 Nevertheless, baseflow in this catchment is sustained throughout the whole year, thus reflecting water
500 delivered through deeper pathways, with residence times larger than the shallow fast flow that
501 predominates during storm events (Schellekens et al., 2004). Chlorite contains ~22 times more Mg
502 than the bulk regolith in molar proportions, is the most abundant Mg-bearing phase in the bedrock
503 (Tables 1, S2), and is more susceptible to dissolution than the kaolinite-rich, Mg-poor regolith at
504 Earth's surface conditions. Therefore, we consider chlorite as the most plausible phase determining
505 the isotopically heavy Mg signature of the stream during baseflow.

506

507 ***Fractionation processes***
508

509 Fractionation models are widely used to describe stable isotope ratios in rivers and calculate
510 fractionation factors associated with weathering reactions (e.g., Dellinger et al., 2015; Georg et al.,
511 2007). The best-known examples are Rayleigh-like systems, where a mineral is dissolving without
512 precipitation of a secondary phase. We develop such a model in the supplementary material, with
513 water in equilibrium with dissolving chlorite as the starting material (Fig. 10a). However, because of
514 the comparatively slow kinetics of silicate dissolution, it is problematic to claim that chlorite
515 dissolution is the main control over the stream [Mg] – δ^{26}Mg on the hourly time scale of the storm

event. Alternatively, the linear trend of δ^{26}Mg vs. [Mg] in the stream (Figs. 10, 11) can be modelled using a mass balance approach (Bouchez et al., 2013; Dellinger et al., 2015), considering the small catchment as an open, flow-through system in which Mg is released to solution by one reaction while it is removed by another (e.g., incorporation into secondary minerals). As with chlorite dissolution, Mg uptake by secondary mineral precipitation is unlikely to control the stream chemistry at the time scale of a single storm event. On the other hand, ion exchange and sorption-desorption reactions are rapid enough to occur over 30 minute time scales and, in fact, ion-exchange has been proposed to be a first order control on stream chemistry (e.g., Berner, 1998; Clow and Mast, 2010) and on Mg isotope fractionation (Jacobson et al., 2010; Opfergelt et al., 2012). Therefore, although we do not have enough evidence to conclusively resolve if sorption or ion exchange are the primary cause of Mg isotope fractionation, we contend these are the only plausible mechanisms capable of fractionating Mg isotopes at the required hourly time scale.

At steady state, all Mg inputs and outputs, as well as their isotopic compositions, are balanced and the Mg isotope composition of the stream can be modelled as:

$$\delta^{26}Mg_{stream} = \delta^{26}Mg_i - \Delta_{i,s}(1 - f_{Mg}) \quad (2)$$

where $\delta^{26}Mg_{stream}$ and $\delta^{26}Mg_i$, are the Mg isotopic compositions of the dissolved load in the stream and of the initial reservoir, respectively, $\Delta_{i,s}$ is the separation factor between the initial reservoir and the stream ($\Delta \approx 1000\ln\alpha$), and f_{Mg} is the fraction of Mg from the initial reservoir. Our data are well explained by this model (Fig. 10b), with separation factors between + 0.95 and +1.35, and the best fit for $\Delta_{i,,s}$ = +1.15 and $\delta^{26}Mg_i$ = + 0.18‰, very close to the average composition of chlorite (+ 0.19 ‰, Table 3). According to this model, the heavy source (f_{Mg}) represents between 80% (baseflow) and 20% (peak of the storm) of the dissolved Mg in the stream (Fig. 10b). The δ^{26}Mg of deep pore water falls within the same fractionation line as the stream (Fig. 10b), as expected if both had inputs from chlorite weathering.

5.2.2 Mg contributions to the stream from different landscape units

543 The δ^{26}Mg of baseflow reflects the input of sources deeper than any of our sampled pore water, likely
544 water flowing through bedrock fractures or at the bedrock-regolith interface where chlorite is actively
545 dissolving (Section 5.2.1). Nonetheless, pore water may influence the δ^{26}Mg signature of the stream
546 during other stages of storm events, as has been found from water composition mixing models and
547 hydrometric studies (Schellekens et al., 2004). The δ^{26}Mg signature of this contribution would depend
548 on the pathways followed by water before reaching the stream, as indicated by our data along the
549 topographic profile showing differing δ^{26}Mg in pore water over a relatively short lateral and vertical
550 distance (Fig. 6).

551 To investigate if the pore water δ^{26}Mg variation in the landscape would affect the stream
552 composition, we performed a simple mass balance assuming that our pore water profiles are
553 representative of the pore water composition by landscape unit in the whole catchment (B1S1= ridges,
554 B1S2 = slopes and B1S4 = valleys):

555 $$\delta^{26}Mg_{PW} = f_r \cdot \delta^{26}Mg_r + f_s \cdot \delta^{26}Mg_s + f_v \cdot \delta^{26}Mg_v \quad (3)$$

556 where $\delta^{26}Mg_{PW}$ is the overall Mg isotopic composition of pore water in the regolith, and *fs, fr, fv* are
557 the fraction of Mg that comes from pore water held in the slopes, the ridges, and the valleys,
558 respectively (Eq. S2). The parameters we used and the estimated fractions of Mg from each landscape
559 unit are summarised in Table 4 and explained in more detail in the supplementary material. We tested
560 the mass-balance Eq. (3) under two scenarios. First, we assume the main contributor to the stream
561 solutes during storm events is water flowing via macropores in the upper 20 cm of the regolith, as
562 proposed by previous studies in the Bisley catchments (Schellekens et al., 2004; McDowell et al.,
563 1992), which we call subsurface shallow flow (SSF). Then we use the same set of equations, but we
564 assume pore water from the entire augerable regolith contributes to the stream Mg (Table 4).

565 Under the first scenario, we estimate that SSF that reaches the stream would have [Mg] = 34.8
566 µM L^{-1} and δ^{26}Mg = – 0.70‰ (Table 4), similar to the δ^{26}Mg of the stream at the peaks of the storm
567 (– 0.74‰), but with a high [Mg] more alike baseflow (45.8 µM L^{-1}, Fig. 11). This apparent
568 contradiction is probably due to the fact that riparian zones in this site are often saturated (Stallard,

2012). Indeed, if we exclude the valley site (B1S4) from Eq. (3) we obtain [Mg] = 21.6 μM L^{-1} and $\delta^{26}Mg_{SSF}$ = − 0.78‰, within error of the δ^{26}Mg of the stream at the peak of the storm and a more reasonable Mg concentration, suggesting that SSF possibly bypasses pore water in the valleys, which have the heaviest δ^{26}Mg (− 0.55‰) at the surface samples of all sites (Fig. 6). Field observations support this argument, as quick flow springs form gullies at slope positions before reaching the valleys (e.g., Schellekens et al., 2004).

Under the assumption of water flow through the entire augerable regolith, we obtain a similar [Mg] than for SSF but higher δ^{26}Mg (− 0.44‰; Table 4). An interesting insight from this model is that whereas in terms of surface the slopes are by far the predominant physiographic unit in the catchment, in terms of dissolved Mg reservoirs ridges are more important due to their deeper regolith and thus higher capacity to store water (Table 4). Figure 11 also shows that if pore water Mg from the whole catchment became well mixed before reaching the stream, it would contribute to the Mg budget during the intermediate stages of the storm. If it remained differentiated by following different pathways to the stream, the ridges would contribute during the intermediate stages and the slopes during the high stages of the storm (Fig. 11).

5.3 Magnesium mass balance of the catchment and weathering rates

Our estimation of the size of the different long-term (annual to decadal scale) Mg pools and fluxes in this catchment are summarised in Table 5. Most of them are in agreement with previously published values (McDowell, 1998; Porder et al., 2015), except the regolith pools, which are somewhat higher due to the fact that other studies only consider the top meter whereas we considered the entire augerable regolith. Among the relatively mobile pools, the exchangeable fraction is by far the largest, followed by the vegetation (Table 5).

Export from watersheds as solid, rather than dissolved, phase may represent an additional source or sink of Mg and fractionate isotopes during ion exchange with the dissolved load in a river

(e.g., Dellinger et al., 2014; Tipper et al., 2012b; Bouchez et al., 2013), and this mechanism is likely involved in the short-term δ^{26}Mg – [Mg] balance of our stream (Section 5.2.1). However, although we did not sample such solid phase components (suspended solids, coarse particulate organic matter, and bed sediment) in our study, the suspended sediment concentrations are very low in the volcaniclastic watersheds of the LCZO, with most dissolved constituents including Mg known to be derived from bedrock weathering or atmospheric deposition at the decadal time scale (Stallard and Murphy, 2012). Likewise, the flux of coarse particulate organic matter (i.e., leaves, wood and other plant material) represents only 0.00242 kg ha^{-1} yr^{-1} of Mg flux out of the Bisley catchments (Heartsill Scalley et al., 2012), which is negligible compared to the 60 kg ha^{-1} yr^{-1} of dissolved Mg flux (McDowell, 1998). Streambed sediments are also unlikely to contribute significant Mg, as the streams in the volcaniclastic catchments of the LCZO are characteristically lined with bedrock, boulders or cobbles, with little bed sediment (Murphy and Stallard, 2012). Finally, ionic exchange or sorption into the regolith before runoff reaches the stream are also unlikely to be an important sink or source of Mg at the decadal time scale, because it is dominated by 1:1 type clays (Buss and White 2012; Dosseto et al., 2012), which have very low cation exchange capacity.

After these considerations, a mass balance for Mg in the whole catchment, assuming there are no water outputs other than the stream, can be written as:

$$Q_p + Q_L + Q_{BR} + Q_{dust} = Q_v + Q \quad (4)$$

where Q_p is openfall, Q_L is litter decomposition, Q_{BR} is the dissolution of the bedrock, Q_{dust} is the dust solid load not included in the openfall samples, Q_v is uptake by vegetation and Q is the stream export. We consider litter decomposition and vegetation uptake to be in steady state (Scatena et al., 1996), and thus Eq. (4) is simplified to:

$$Q_p + Q_{BR} + Q_{dust} = Q \quad (5)$$

Substituting the values of Q_p, Q_{dust} and Q from Table 5 into Eq. (5) and solving for Q_{BR}, we can estimate a flux of 35 kg ha^{-1} yr^{-1} (or 1440 mol ha^{-1} yr^{-1}) of Mg from bedrock dissolution, making

it the largest input to the stream (Table 5) as has been found in larger streams within the LZCO (Stallard and Murphy, 2012, and references therein). This result highlights the importance of deeper critical zone pathways for Mg fluxes in areas covered by thick, highly leached regolith. The fact that [Mg] in pore water and the exchangeable fraction within the rooting zone are dominated by rain inputs (Section 5.1), whereas the [Mg] in the stream is dominated by bedrock dissolution at depth (Section 5.2.1), is consistent with a decoupling between the water that is taken up by the vegetation, and the water that reaches the streams (McDonell, 2014; Evaristo et al., 2015), although the source of Mg seems to be even deeper than suggested by $\delta^{18}O$ and $\delta^{2}H$ studies (Evaristo et al., 2016).

Using the abundance of chlorite in the bedrock (Buss et al., 2013), its Mg content (Table S2), and assuming all Mg-bearing minerals are dissolving either congruently or have non-Mg bearing clays as the product (e.g., kaolinite), we can use the bedrock dissolution Mg flux (Table 5) to estimate that chlorite dissolves roughly at 19 kg ha^{-1} yr^{-1} (763 mol ha^{-1} yr^{-1}) in this catchment. Because of the several assumptions we made, these rates are likely to represent upper limits. Nevertheless, as a first order approximation, our chlorite weathering rate is an order of magnitude faster than the highest published watershed-scale dissolution rates for other ferromagnesian silicates (biotite = 26 mol ha^{-1} yr^{-1}, Mast et al., 1990; hornblende = 24 mol ha^{-1} yr^{-1}, Williams et al., 1993). This result illustrates that chemical weathering rates in tropical critical zones are fast relative to rates in temperate zones (e.g., Dosseto et al., 2012), leading to their comparatively greater contribution to global silicate weathering fluxes to the oceans (Stallard and Edmond, 1983; Meybeck, 1987; Rad et al., 2007).

5.4 Implications for the evolution of Mg isotope exports from silicate catchments

Our results indicate that the flux of Mg through deeper pathways in the critical zone could be comparatively more important than through shallow pathways in highly weathered sites (Sections 5.2.1 and 5.3), but we note that variable degrees of weathering (Fig. 3b) may lead to differences in pore water $\delta^{26}Mg$ within the same catchment (Fig. 6). This relationship between $\delta^{26}Mg$ and degree of weathering is consistent with previous work (Fig. 12). Although more studies are clearly needed,

especially at intermediate weathering stages, here we put forward a conceptual model of the evolution of the Mg isotopic composition of silicate catchments based on the relation between δ^{26}Mg and regolith chemical depletion (CIA) observed thus far (Fig. 12):

1) Incipient weathering stage (fractured bedrock or thin, young soils; CIA<20). The rock has just been exposed to chemical weathering (Tipper et al., 2012b), and fast-reacting minerals are still available (Trostle et al., 2014). The regolith has a Mg isotopic composition similar to the bedrock. Dissolution of fast-reacting primary minerals is the main control on the δ^{26}Mg signature of the streams, which thus can be heavier or lighter than the bedrock.

2) Advanced weathering stage (bedrock-saprolite interfaces on fully developed profiles; 50<CIA<80). The regolith is constituted mainly of 2:1 secondary clays, oxides, and some remaining primary minerals, and has Mg isotope ratios heavier than the bedrock (Bolou-Bi et al., 2012; Opfergelt et al., 2012). Atmospheric inputs start to be an important source of Mg (Opfergelt et al., 2012). The streams have lower δ^{26}Mg than the bedrock they drain due to secondary minerals preferentially holding ^{26}Mg, but they can reflect the dissolution of primary minerals during baseflow.

3) Extreme weathering stage (deep, highly weathered regolith; CIA>80). The regolith has very low cation exchange capacity (CEC) because it is comprised mostly of 1:1 clays and Fe, Mn, Al (hydr)oxides below their point of zero charge. Atmospheric inputs, changes in redox conditions within the regolith, and hydrological factors become comparatively more important (this work; Dessert et al., 2015; Liu et al., 2014). The bulk regolith has a high δ^{26}Mg, but little influence on the δ^{26}Mg of the streams. The δ^{26}Mg signature of the streams is thus very similar to the previous stage, with a δ^{26}Mg signature similar or slightly higher than the bedrock during baseflow and δ^{26}Mg fluctuations reflecting varying rain inputs.

We also note that the Mg isotopic composition of streams and rivers remains essentially constant after about 75% chemical depletion (CIA) of the regolith, despite continuing increase in the regolith δ^{26}Mg values (Fig.12).

672 Ultimately, the δ^{26}Mg of the streams will depend on access to reactive minerals and flow paths,
673 which in turn, largely depend on the physical properties of the catchment. Our study thus highlights
674 the need for a good understanding of the local geo-hydrological setting to narrow the geochemical
675 hypotheses, while also illustrating how geochemical observations (Mg isotope ratios in this case) can,
676 in turn, give insight into the water pathways and on the subsurface architecture of the critical zone.

677

678 ## 6. CONCLUSIONS

679 To better understand the effects of critical zone processes on Mg concentrations and the Mg isotopic
680 signature of streams in the tropics, we studied a well constrained, highly weathered volcaniclastic
681 catchment in the Luquillo Critical Zone Observatory, Puerto Rico. As hypothesised, the general depth
682 trend of pore water δ^{26}Mg is consistent with rain inputs at the surface and bedrock weathering at the
683 base of the profile, despite the fact that this trend is not clearly expressed in rain-corrected Mg
684 concentrations. Contrary to what we expected, most Mg in pore water is sourced from rain,
685 highlighting the importance of atmospheric inputs to nutrient budgets in tropical sites. However,
686 binary mixing between rainfall and weathering end-members is insufficient to explain the relationship
687 between [Mg] and δ^{26}Mg in pore water, indicating that a fractionation process is also taking place,
688 interpreted to be the preferential retention of heavy ^{26}Mg into secondary minerals. A separate
689 fractionation process is evidenced by a ~ 0.11‰ shift in δ^{26}Mg towards heavier values at ~ 1 m depth,
690 coinciding with redoximorphic features and a correlation between [Mg] and δ^{26}Mg in the bulk
691 regolith and the exchangeable fraction with Fe(III)-(hydr)oxide contents; we interpret this isotopic
692 excursion to represent the release of sorbed, isotopically heavy Mg from Fe(III)-(hydr)oxides during
693 periodic reducing conditions. Overall, pore water [Mg] and δ^{26}Mg data are consistent with control by
694 rainwater infiltration and geochemical reactions within the regolith on the short - term.

695 The relative importance of the Mg-controlling processes in shallow samples differs over the
696 time scales studied. Whereas [Mg] and δ^{26}Mg data in pore water and the exchangeable fraction
697 indicate that rain is the predominant source of Mg in the surface up to approximately decadal time

scales, at the longer time scale represented by the bulk regolith dust is the dominant Mg source to the shallow critical zone. Bedrock weathering is the predominant source of Mg at depth over all the time scales.

Pore water depth profiles along a topo-sequence show the same trend from lower to higher δ^{26}Mg and [Mg] contents with increasing depth, but shallower, less-weathered sites have higher [Mg] and δ^{26}Mg than the ridgetop site. We used these values to estimate the composition of pore water from the whole catchment exported to the stream under two flow path scenarios. These calculations suggest that *i*) flow paths that export Mg to the stream largely bypass the valley regolith; *ii)* shallow flow may contribute to the stream during the peaks of storm events but not during base flow; and *iii)* whereas slopes are the largest unit of the catchment by area, ridges are the largest pore water Mg reservoir.

During baseflow, the stream is isotopically heavier than pore water from any depth and the bulk bedrock, indicating that sources other than rain, bulk bedrock dissolution and pore water contribute Mg to the stream. *In situ* analysis of the δ^{26}Mg of the bedrock minerals indicated preferential chlorite dissolution at depth as the most plausible isotopically heavy source of Mg to the stream. This result underscores a need for a better understanding of deep critical zone processes, which are comparatively more important for watershed chemical budgets when surficial pools are exhausted by extreme weathering.

Altogether, our study highlights the importance of atmospheric inputs of nutrients to tropical ecosystems (rain on shorter time scales and dust on longer time scales), whereas the dissolution of primary minerals in the deep critical zone dominates Mg fluxes and the Mg isotope signature of the stream, even at the advanced weathering stage of this catchment.

ACKNOWLEDGMENTS

We are grateful to Jane Willenbring (Univ. of Penn.) for providing the stream water samples and Laura Liermann (Penn. State Univ.) for providing the samples for trace element analysis in surficial bulk regolith. We also thank the US Forest Service for logistical support; Manuel Rosario Torres (USGS) for help in the field; John Fitzpatrick (USGS), Chris Coath (Univ. of Bristol) and the Bristol Isotope Group for lab assistance; Miguel Leon (LCZO information manager) for GIS assistance; and Laura Robinson (Univ. of Bristol) and Edward Tipper (Univ. of Cambridge) for helpful discussions. Friedhelm von Blanckenburg is thanked for infrastructure support for analyses at GFZ Potsdam. Our manuscript was improved by the useful reviews of Josh Wimpenny, Xiao-Ming Liu and an anonymous reviewer, and to the editorial handling of Fangzhen Teng. M. Chapela was supported by a Consejo Nacional de Ciencia y Tecnología (Conacyt) PhD scholarship. H.L. Buss acknowledges support of the NSF-Luquillo Critical Zone (NSF EAR-0722476 and EAR-1331841) and an FP-7 Marie Curie International Incoming Fellowship from the European Commission. P. Pogge von Strandmann was funded by a NERC Advanced Research Fellowship NE/I020571/2.

References

Balistrieri, L.S., Borrok, D.M., Wanty, R.B., Ridley, W.I., 2008. Fractionation of Cu and Zn isotopes during adsorption onto amorphous Fe(III) oxyhydroxide: Experimental mixing of acid rock drainage and ambient river water. Geochimica et Cosmochimica Acta 72, 311-328.

Bernasconi, S.M., Bauder, A., Bourdon, B., Brunner, I., Bünemann, E., Chris, I., Derungs, N., Edwards, P., Farinotti, D., Frey, B., Frossard, E., Furrer, G., Gierga, M., Göransson, H., Gülland, K., Hagedorn, F., Hajdas, I., Hindshaw, R., Ivy-Ochs, S., Jansa, J., Jonas, T., Kiczka, M., Kretzschmar, R., Lemarchand, E., Luster, J., Magnusson, J., Mitchell, E.A.D., Venterink, H.O., Plötze, M., Reynolds, B., Smittenberg, R.H., Stähli, M., Tamburini, F., Tipper, E.T., Wacker, L., Welc, M., Wiederhold, J.G., Zeyer, J., Zimmermann, S., Zumsteg, A., 2011. Chemical and Biological Gradients along the Damma Glacier Soil Chronosequence, Switzerland. Vadose Zone Journal 10, 867-883.

749 Berner, R.A., 1995. Chemical weathering and its effect on atmospheric CO2 and climate, in: White, A.F.,
750 Brantley, S.L. (Eds.), Chemical Weathering Rates of Silicate Minerals. Mineralogical Society of America,
751 Washington, D.C.

752 Berner, R.A., 1998. The carbon cycle and carbon dioxide over Phanerozoic time: the role of land plants.
753 Philosophy Transactions Royal Society B: Biology Sciences 353, 75–82.

754 Berner, R.A., Berner, E.K., 1997. Silicate weathering and climate, in: Ruddiman, W.F. (Ed.), Tectonic Uplift
755 and Climate Change. Plenum Press, New York, pp. 353-364.

756 Berner, R.A., Lasaga, A.C., Garrels, R.M. (1983) The carbonate-silicate geochemical cycle and its effect on
757 atmospheric carbon dioxide over the past 100 million years. American Journal of Science 283, 641-683.

758 Black, J.R., Epstein, E., Rains, W.D., Yin, Q.-z., Casey, W.H., 2008. Magnesium-Isotope Fractionation During
759 Plant Growth. Environmental Science & Technology 42, 7831-7836.

760 Bolou-Bi, E., Vigier, N., Poszwa, A., Boudot, J.-P., Dambrine, E., 2012. Effects of biogeochemical processes on
761 magnesium isotope variations in a forested catchment in the Vosges Mountains (France). Geochimica et
762 Cosmochimica Acta 87, 341-355.

763 Bolou-Bi, E.B., Poszwab, A., Leyvalb, C., Vigier, N., 2010. Experimental determination of magnesium isotope
764 fractionation during higher plant growth. Geochimica et Cosmochimica Acta 74, 2523-2537.

765 Bonell, M., 2005. Runoff generation in tropical forests, in: Bonell, M., Bruijnzeel, L.A. (Eds.), Forests, Water
766 and People in the Humid Tropics Past, Present and Future Hydrological Research for Integrated Land and Water
767 Management. Cambridge University Press, pp. 314-406.

768 Bouchez, J., von Blanckenburg, F., Schuessler, J.A., 2013. Modeling novel stable isotope ratios in the
769 weathering zone. American Journal of Science 313, 267-308.

770 Brady, N.C., Weil, R.R., 2007. The nature and properties of soils, 14 ed. Prentice Hall, Upper Saddle River, NJ.

771 Brantley, S.L., Lebedeva, M., 2011. Learning to Read the Chemistry of Regolith to Understand the Critical
772 Zone. Annual Review of Earth and Planetary Sciences 39, 387-416.

773 Brenot, A., Cloquet, C., Vigier, N., Carignan, J., France-Lanord, C., 2008. Magnesium isotope systematics of
774 the lithologically varied Moselle river basin, France. Geochimica et Cosmochimica Acta 72, 5070-5089.

775 Briggs, R.P., 1973. The lower Cretaceous Figuera Lava and Fajardo Formation in the stratigraphy of
776 northeastern Puerto Rico. U.S. Geological Survey Bulletin 1372-G.

777 Bullen, T.D., 2014. Metal stable isotopes in weathering and hydrology: Chapter 10. Treatise on Geochemistry 7,
778 329-359.

779 Buss, H.L., White, A., 2012. Weathering Processes in the Icacos and Mameyes Watersheds in Eastern Puerto
780 Rico, in: Murphy, S.F.S., R. (Ed.), Water Quality and Landscape Processes of Four Watersheds in Eastern
781 Puerto Rico. US Geological Survey, Reston, Virginia, pp. 249-287.

782 Buss, H.L., Chapela Lara, M., Moore, O.W., Kurtz, A.C., Schulz, M.S., White, A.F., 2017. Lithological
783 influences on contemporary and long-term regolith weathering at the Luquillo Critical Zone Observatory.
784 Geochimica et Cosmochimica Acta 196, 224-251.

785 Buss, H.L., Brantley, S.L., Scatena, F.N., Bazilievskaya, E.A., Blum, A.E., Schulz, M., Jiménez, R., White,
786 A.F., Rother, G., Cole, D., 2013. Probing the deep critical zone beneath the Luquillo Experimental Forest,
787 Puerto Rico. Earth Surface Processes and Landforms 38, 1170-1186.

788 Chapela Lara, M., Buss, H.L., Pogge von Strandmann, P.A.E., Dessert, C., Gaillardet, J., 2014. Controls on the
789 Mg cycle in the tropics: insights from a case study at the Luquillo Critical Zone Observatory. Procedia Earth
790 and Planetary Science 10, 200-203.

791 Chapin, F.S., Zavaleta, E.S., Eviner, V.T., Naylor, R.S., Vitousek, P.M., Reynolds, H.L., Hooper, D.U.,
792 Lavorel, S., Sala, O.E., Hobbie, S.E., Mack, M.C., Díaz, S., 2010. Consequences of changing biodiversity.
793 Nature 405, 234-242.

794 Clergue, C., Dellinger, M., Buss, H.L., Gaillardet, J., Benedetti, M.F., Dessert, C., 2015. Influence of
795 atmospheric deposits and secondary minerals on Li isotopes budget in a highly weathered catchment,
796 Guadeloupe (Lesser Antilles). Chemical Geology 414, 28-41.

797 Clow, D.W., Mast, M.A., 2010. Mechanisms for chemostatic behavior in catchments: implications for CO2
798 consumption by mineral weathering. Chemical Geology 269, 40–51.

799 Dellinger, M., Gaillardet, J., Bouchez, J., Calmels, D., Louvat, P., Dosseto, A., Gorge, C., Alanoca, L., Maurice,
800 L., 2015. Riverine Li isotope fractionation in the Amazon River basin controlled by the weathering regimes.
801 Geochimica et Cosmochimica Acta 164, 71-93.

802 Dellinger, M., Gaillardet, J., Bouchez, J., Calmels, D., Galy, V., Hilton, R.G., Louvat, P., France-Lanord, C.,
803 2014. Lithium isotopes in large rivers reveal the cannibalistic nature of modern continental weathering and
804 erosion. Earth and Planetary Science Letters 401, 359-372.

805 Dessert, C., Lajeunesse, E., Lloret, E., Clergue, C., Crispi, O., Gorge, C., Quidelleur, X., 2015. Controls on
806 chemical weathering on a mountainous volcanic tropical island: Guadeloupe (French West Indies). Geochimica
807 et Cosmochimica Acta 171, 216-237.

808 Dosseto, A., Buss, H.L., Suresh, P.O., 2012. Rapid regolith formation over volcanic bedrock and implications
809 for landscape evolution. Earth and Planetary Science Letters 337-338, 47-55.

810 Elsenbeer, H., 2001. Hydrologic flowpaths in tropical rainforest soilscapes—a review. Hydrological Processes
811 15, 1751-1759.

812 Evaristo, J., Jasechko, S., McDonnell, J.J., 2015. Global separation of plant transpiration from groundwater and
813 streamflow. Nature 525, 91-94.

814 Evaristo, J., McDonnell, J.J., Scholl, M.A., Bruijnzeel, L.A., Chun, K.P., 2016. Insights into plant water uptake
815 from xylem-water isotope measurements in two tropical catchments with contrasting moisture conditions.
816 Hydrological Processes, doi: 10.1002/hyp.10841.

817 Fagerbakke, K. M., Norland, S., Heldal M., 1999. The inorganic ion content of native aquatic bacteria. Can. J.
818 Microbiol. 45, 304–311.

819 Foster, G.L., Pogge von Strandmann, P.A.E., Rae, J.W.B., 2010. Boron and magnesium isotopic composition of
820 seawater. Geochemistry, Geophysics, Geosystems 11, Q08015, doi:10.1029/2010GC003201.

821 Frierdich, A.J., Catalano, J.G., 2012. Controls on Fe(II)-Activated Trace Element Release from Goethite and
822 Hematite. Environmental Science & Technology 46, 1519-1526.

823 Galy, A.O., Janney, Y.P., Williams, R., Cloquet, C., Alard, O., Halicz, L., Wadhwa, M., Hutcheon, I., Ramon,
824 E., Carignan, J., 2003. Magnesium isotope heterogeneity of the isotopic standard SRM980 and new reference
825 materials for magnesium isotope ratio measurements. Journal of Analytical Atomic Spectrometry 18, 1352-
826 1356.

827 Georg, R.B., Reynolds, B.C., West, A.J., Burton, K.W., Halliday, A.N., 2007. Silicon isotope variations
828 accompanying basalt weathering in Iceland. Earth and Planetary Science Letters 261, 476-490.

Gioda, A., Mayol-Bracero, O.L., Scatena, F.N., Weathers, K.C., Mateus, V.L., McDowell, W.H., 2013. Chemical constituents in clouds and rainwater in the Puerto Rican rainforest: Potential sources and seasonal drivers. Atmospheric Environment 68, 208-220.

Goller, R., Wilcke, W., Leng, M.J., Tobschall, H.J., Wagner, K., Valarezo, C., Zech, W., 2005. Tracing water paths through small catchments under a tropical montane rain forest in south Ecuador by an oxygen isotope approach. Journal of Hydrology 308, 67-80.

Gonzalez, G., 2011a. Bisley daily rainfall (Bisley weekly environmental data). Long Term Ecological Research Network. http://dx.doi.org/10.6073/pasta/f9ce74b63495a242128fb5f93f5ebdf5. Accessed 27/05/2015.

Gonzalez, G., 2011b. Daily streamflow (Bisley area, 5 stations: Q1, Q2, Q3, Sabana, Puente Roto). Long Term Ecological Research Network. http://dx.doi.org/10.6073/pasta/de3e88a857d427bb82edcef0bdd21e8c. Accessed 27/05/2015.

Heartsill Scalley, T., Scatena, F.N., Moya, S., Lugo, A.E., 2012. Long-term dynamics of organic matter and elements exported as coarse particulates from two Caribbean montane watersheds. Journal of Tropical Ecology 28, 127-139.

Heldal M., Norland S., Erichsen E. S., Larsen A., Thingstand F. and Bratbak G., 2012. Mg2+ as an indicator of nutritional status in marine bacteria. ISME J. 6, 2524–2530.

Henriet, C., Bodarwé, L., Dorel, M., Draye, X., Delvaux, B., 2008. Leaf silicon content in banana (Musa spp.) reveals the weathering stage of volcanic ash soils in Guadeloupe. Plant Soil 313, 71-82.

Herwitz, S.R., Muhs, D.R., Prospero, J.M., Mahan, S., Vaughn, B., 1996. Origin of Bermuda's clay-rich Quaternary paleosols and their paleoclimatic significance. Journal of Geophysical Research: Atmospheres 101, 23389-23400.

Huang, K.J., Teng, F.Z., Wei, G.J., Ma, J.L., Bao, Z.Y., 2012. Adsorption- and desorption-controlled magnesium isotope fractionation during extreme weathering of basalt in Hainan Island, China. Earth and Planetary Science Letters 2012, 73-83.

Huffaker, L., 2002. Soil Survey of Caribbean National Forest and Luquillo Experimental Forest, Commonwealth of Puerto Rico. USDA-NRCS.

855 Jacobson, A.D., Zhang, Z., Lundstrom, C., Huang, F., 2010. Behavior of Mg isotopes during dedolomitization
856 in the Madison Aquifer, South Dakota. Earth and Planetary Science Letters 297, 446–452.

857 Johnston, M.H., 1992. Soil-vegetation relationships in a tabonuco forest community in the Luquillo Mountains
858 of Puerto Rico. Journal of Tropical Ecology 8, 253-263.

859 Jordan, C.F., Herrera, R., 1981. Tropical Rain Forests: Are Nutrients Really Critical? The American Naturalist
860 117, 167-180.

861 Kump, L.R., Brantley, S.L., Arthur, M.A., 2000. Chemical weathering, atmospheric CO2 and climate. Ann. Rev
862 of Earth and Planetary Sciences 28, 611-667.

863 Kurtz, A.C., Lugolobi, F., Salvucci, G., 2011. Germanium-silicon as a flowpath tracer: Application to the Rio
864 Icacos watershed. Water Resources Research 47, W06516.

865 Kurtz, A.C., Derry, L.A., Chadwick, O.A., Alfano, M.J., 2000. Refractory element mobility in volcanic soils.
866 Geology 28, 683-686.

867 Langmuir, C.H., Vocke, R.D., Hanson, G.H., Hart, S.R., 1978. A general mixing equation with applications to
868 Icelandic basalts. Earth and Planetary Science Letters 37, 380-392.

869 Li, W., Beard, B.L., Li, C., Johnson, C.M., 2014. Magnesium isotope fractionation between brucite [Mg(OH)2]
870 and Mg aqueous species: Implications for silicate weathering and biogeochemical processes. Earth and
871 Planetary Science Letters 394, 82-93.

872 Li, W.-Y., Teng, F.-Z., Ke, S., Rudnick, R.L., Gao, S., Wu, F.-Y., Chappell, B.W., 2010. Heterogeneous
873 magnesium isotopic composition of the upper continental crust. Geochimica et Cosmochimica Acta 74, 6867-
874 6884.

875 Liermann, L.J., Albert, I., Buss, H.L., Minyard, M., Brantley, S.L., 2014. Relating Microbial Community
876 Structure and Geochemistry in Deep Regolith Developed on Volcaniclastic Rock in the Luquillo Mountains,
877 Puerto Rico. Geomicrobiology Journal 32, 494-510.

878 Ling, M.X., Sedaghatpour, F., Teng, F.Z., Hays, P.D., Strauss, J., Sun, W., 2011. Homogeneous magnesium
879 isotopic composition of seawater: an excellent geostandard for Mg isotope analysis. Rapid Communications in
880 Mass Spectrometry 25, 2828-2836.

881 Liptzin, D., Silver, W.L., 2009. Effects of carbon additions on iron reduction and phosphorus availability in a
882 humid tropical forest soil. Soil Biology & Biochemistry doi:10.1016/j.soilbio.2009.05.013.

883 Liu, X.-M., Teng, F.Z., Rudnick, R.L., McDonough, W.F., Cummings, M.L., 2014. Massive magnesium
884 depletion and isotope fractionation in weathered basalts. Geochimica et Cosmochimica Acta 135, 336-349.

885 Liu, S.-A., Teng, F.-Z., He, Y., Ke, S., Li, S., 2010. Investigation of magnesium isotope fractionation during
886 granite differentiation: Implication for Mg isotopic composition of the continental crust. Earth and Planetary
887 Science Letters 297, 646-654.

888 Ma, L., Teng, F.-Z., Jin, L., Ke, S., Yang, W., Gu, H.-O., Brantley, S.L., 2015. Magnesium isotope fractionation
889 during shale weathering in the Shale Hills Critical Zone Observatory: Accumulation of light Mg isotopes in
890 soils by clay mineral transformation. Chemical Geology 397, 37-50.

891 Ma, J.-L., Wei, G.-J., Xu, Y.-G., Long, W.-G., Sun, W.-D., 2007. Mobilization and re-distribution of major and
892 trace elements during extreme weathering of basalt in Hainan Island, South China. Geochimica et
893 Cosmochimica Acta 71, 3223-3237.

894 Mast, M.A., Drever, J.I., Baron, J., 1990. Chemical Weathering in the Loch Vale Watershed, Rocky Mountain
895 National Park, Colorado. Water Resources Research 26, 2971-2978.

896 Mavromatis, V., Pearce, C.R., Shirokova, L.S., Bundeleva, I.A., Pokrovsky, O.S., Benezeth, P., Oelkers, E.H.,
897 2012. Magnesium isotope fractionation during hydrous magnesium carbonate precipitation with and without
898 cyanobacteria. Geochimica et Cosmochimica Acta 76, 161-174.

899 McDonell, J.J., 2014. The two water worlds hypothesis: Ecohydrological separation of water between streams
900 and trees? WIREs Water 1, 323-329.

901 McDowell, W.H., 1998. Internal nutrient fluxes in a Puerto Rican rain forest. Journal of Tropical Ecology 14,
902 521-536.

903 McDowell, W.H., 2010. Chemistry of stream water from the Luquillo Mountains. Long Term Ecological
904 Research Network. http://dx.doi.org/10.6073/pasta/63e41fb1bb1bf05d7cdca90c55769fa4. Accessed 27/05/2015.

905 McDowell, W.H., 2012. Chemistry of rainfall and throughfall from El Verde and Bisley. Long Term Ecological
906 Research Network. http://dx.doi.org/10.6073/pasta/d113d7ac3a23d3a9cbdc0824789640e7. Accessed
907 27/05/2015.

908 McDowell, W.H., Asbury, C.E., 1994. Export of carbon, nitrogen, and major ions from three tropical montane
909 watersheds. Limnology and Oceanography 39, 111-125.

910 McDowell, W., Bowden, W., Asbury, C., 1992. Riparian nitrogen dynamics in two geomorphologically distinct
911 tropical rain forest watersheds: subsurface solute patterns. Biogeochemistry 18, 53-75.

912 Meybeck, M., 1987. Global chemical weathering of surficial rocks estimated from dissolved river loads.
913 American Journal of Science 287, 401-428.

914 Mikutta, C., Wiederhold, J.G., Cirpka, O.A., Hofstetter, T.B., Bourdon, B., Gunten, U.V., 2009. Iron isotope
915 fractionation and atom exchange during sorption of ferrous iron to mineral surfaces. Geochimica et
916 Cosmochimica Acta 73, 1795-1812.

917 Murphy, S.F., and Stallard, R.F., eds., 2012, Water quality and landscape processes of four watersheds in
918 eastern Puerto Rico: U.S. Geological Survey Professional Paper 1789, 292 pp.

919 Oelkers, E.H., Benning, L.G., Lutz, S., Mavromatis, V., Pearce, C.R., Plümper, O., 2015. The efficient long-
920 term inhibition of forsterite dissolution by common soil bacteria and fungi at Earth surface conditions.
921 Geochimica et Cosmochimica Acta 168, 222-235.

922 Oeser, M., Weyer, S., Horn, I., Schuth, S., 2014. High-Precision Fe and Mg Isotope Ratios of Silicate Reference
923 Glasses Determined In Situ by Femtosecond LA-MC-ICP-MS and by Solution Nebulisation MC-ICP-MS.
924 Geostandards and Geoanalytical Research 38, 311-328.

925 Opfergelt, S., Burton, K.W., Georg, R.B., West, A.J., Guicharnaud, R.A., Sigfusson, B., Siebert, C., Gislason,
926 S.R., Halliday, A.N., 2014. Magnesium retention on the soil exchange complex controlling Mg isotope
927 variations in soils, soil solutions and vegetation in volcanic soils, Iceland. Geochimica et Cosmochimica Acta
928 125, 110-130.

929 Opfergelt, S., Georg, R.B., Delvaux, B., Cabidoche, Y.-M., Burton, K.W., Halliday, A.N., 2012. Mechanisms of
930 magnesium isotope fractionation in volcanic soil weathering sequences, Guadeloupe. Earth and Planetary
931 Science Letters 341-344, 176-185.

932 Ostertag, R., Scatena, F.N., Silver, W.L., 2003. Forest Floor Decomposition Following Hurricane Litter Inputs
933 in Several Puerto Rican Forests. Ecosystems 6, 261-273.

934 Pedersen, H.D., Postma, D., Jakobsen, R., Larsen, O., 2005. Fast transformation of iron oxyhydroxides by the
935 catalytic action of aqueous Fe(II). Geochimica et Cosmochimica Acta 69, 3967-3977.

936 Peretyazhko, T., Sposito, G., 2005. Iron(III) reduction and phosphorous solubilization in humid tropical forest
937 soils. Geochimica et Cosmochimica Acta 69, 3643-3652.

938 Pett-Ridge, J., 2009. Contributions of dust to phosphorus cycling in tropical forests of the Luquillo Mountains,
939 Puerto Rico. Biogeochemistry 94, 63-80.

940 Pett-Ridge, J.C., Derry, L.A., Kurtz, A.C., 2009. Sr isotopes as a tracer of weathering processes and dust inputs
941 in a tropical granitoid watershed, Luquillo Mountains, Puerto Rico. Geochimica et Cosmochimica Acta 73, 25-
942 43.

943 Pogge von Strandmann, P.A.E., Dohmen, R., Marschall, H.R., Schumacher, J.C., Elliott, T., 2015. Extreme
944 Magnesium Isotope Fractionation at Outcrop Scale Records the Mechanism and Rate at which Reaction Fronts
945 Advance. Journal of Petrology 56, 33-58.

946 Pogge von Strandmann, P.A.E., Opfergelt, S., Lai, Y.-J., Sigfusson, B., R.Gislason, S., Burton, K.W., 2012.
947 Lithium, magnesium and silicon isotope behaviour accompanying weathering in a basaltic soil and pore water
948 profile in Iceland. Earth and Planetary Science Letters 339-340, 11-23.

949 Pogge von Strandmann, P.A.E., Elliott, T., Marschall, H.R., Coath, C., Lai, Y.-J., Jeffcoate, A.B., Ionov, D.A.,
950 2011. Variations of Li and Mg isotope ratios in bulk chondrites and mantle xenoliths. Geochimica et
951 Cosmochimica Acta 75, 5247-5268.

952 Pokrovsky, O.S., Viers, J., Freydier, R., 2005. Zinc stable isotope fractionation during its adsorption on oxides
953 and hydroxides. Journal of Colloid and Interface Science 291, 192-200.

954 Porder, S., Johnson, A.H., Xing, H.X., Brocard, G., Goldsmith, S., Pett-Ridge, J., 2015. Linking
955 geomorphology, weathering and cation availability in the Luquillo Mountains of Puerto Rico. Geoderma 249–
956 250, 100-110.

957 Price, J.R., Velbel, M.A., 2003. Chemical weathering indices applied to weathering profiles developed on
958 heterogeneous felsic metamorphic parent rocks, pp. 397-416.

959 Rad, S.D., Allègre, C.J., Louvat, P., 2007. Hidden erosion on volcanic islands. Earth and Planetary Science
960 Letters 262, 109-124.

961 Reid, E.A., Reid, J.S., Meier, M.M., Dunlap, M.R., Cliff, S.S., Broumas, A., Perry, K., Maring, H., 2003.
962 Characterization of African dust transported to Puerto Rico by individual particle and size segregated bulk
963 analysis. Journal of Geophysical Research: Atmospheres 108.

964 Ryu, J.S., Jacobson, A.D., Holmden, C., Lundstrom, C., Zhang, Z., 2011. The major ion, □44/40Ca, □44/42Ca,
965 and □26/24Mg geochemistry of granite weathering at pH = 1 and T=25 C: power-law processes and the relative
966 reactivity of minerals. Geochimica et Cosmochimica Acta 75, 6004-6026.

967 Scatena, F.N., 1989. An introduction to the physiography and history of the Bisley Experimental Watersheds in
968 the Luquillo Mountains of Puerto Rico. USDA Forest Service, General Technical Report SO-72, p. 22.

969 Scatena, F.N., Moya, S., Estrada, C., Chinea, J.D., 1996. The First Five Years in the Reorganization of
970 Aboveground Biomass and Nutrient Use Following Hurricane Hugo in the Bisley Experimental Watersheds,
971 Luquillo Experimental Forest, Puerto Rico. Biotropica 28, 424-440.

972 Scatena, F.N., Silver, W., Siccama, T., Johnson, A., Sanchez, M.J., 1993. Biomass and Nutrient Content of the
973 Bisley Experimental Watersheds, Luquillo Experimental Forest, Puerto Rico, Before and After Hurricane Hugo,
974 1989. Biotropica 25, 15-27.

975 Schellekens, J., Scatena, F.N., Bruijnzeel, L.A., van Dijk, A.I.J.M., Groen, M.M.A., van Hogezand, R.J.P.,
976 2004. Stormflow generation in a small rainforest catchment in the Luquillo Experimental Forest, Puerto Rico.
977 Hydrological Processes 18, 505-530.

978 Schmitt, A.D., Vigier, N., Lemarchand, D., Millot, R., Stille, P., Chabaux, F., 2012. Processes controlling the
979 stable isotope compositions of Li, B, Mg and Ca in plants, soils and waters: A review. Comptes Rendus
980 Geoscience 344, 704-722.

981 Schuessler, J.A., von Blanckenburg, F., 2014. Testing the limits of micro-scale analyses of Si stable isotopes by
982 femtosecond laser ablation multicollector inductively coupled plasma mass spectrometry with application to
983 rock weathering. Spectrochimica Acta Part B: Atomic Spectroscopy 98, 1-18.

984 Shen, B., Jacobsen, B., Lee, C.-T.A., Yin, Q.-Z., Morton, D.M., 2009. The Mg isotopic systematics of
985 granitoids in continental arcs and implications for the role of chemical weathering in crust formation.
986 Proceedings of the National Academy of Sciences 106, 20652-20657.

Stallard, R., 2012. Weathering, Landscape Equilibrium, and Carbon in Four Watersheds in Eastern Puerto Rico, in: Murphy, S.F.S., R.F. (Ed.), Water Quality and Landscape Processes of Four Watersheds in Eastern Puerto Rico. US Geological Survey, Reston, Virginia, pp. 199-262.

Stallard, R.F., 2001. Possible Environmental Factors Underlying Amphibian Decline in Eastern Puerto Rico: Analysis of U.S. Government Data Archives. Conservation Biology 15, 943-953.

Stallard, R.F., Edmond, J.M., 1983. Geochemistry of the Amazon: 2. The influence of the geology and weathering environment on the dissolved load. Journal of Geophysical Research 88, 9671-9688.

Stallard, R.F., Murphy, S.F., 2012. Water Quality and Mass Transport in Four Watersheds in Eastern Puerto Rico, in: Murphy, S.F., Stallard, R.F. (Eds.), Water Quality and Landscape Processes of Four Watersheds in Eastern Puerto Rico. USGS, pp. 113-151.

Stoll, B., Jochum, K.P., Herwig, K., Amini, M., Flanz, M., Kreuzburg, B., Kuzmin, D., Willbold, M., Enzweiler, J., 2008. An Automated Iridium-Strip Heater for LA-ICP-MS Bulk Analysis of Geological Samples. Geostandards and Geoanalytical Research 32, 5-26.

Teng, F.-Z., Li, W.-Y., Ke, S., Yang, W., Liu, S.-A., Sedaghatpour, F., Wang, S.-J., Huang, K.-J., Hu, Y., Ling, M.-X., Xiao, Y., Liu, X.-M., Li, X.-W., Gu, H.-O., Sio, C.K., Wallace, D.A., Su, B.-X., Zhao, L., Chamberlin, J., Harrington, M., Brewer, A., 2015. Magnesium Isotopic Compositions of International Geological Reference Materials. Geostandards and Geoanalytical Research 39, 329-339.

Teng, F.Z., Li, W.Y., Rudnick, R.L., Gardner, L.R., 2010. Contrasting lithium and magnesium isotope fractionation during continental weathering. Earth and Planetary Science Letters 300, 63-71.

Thompson, A., Chadwick, O.A., Rancourt, D.G., Chorover, J., 2006. Iron-oxide crystallinity increases during soil redox oscillations. Geochimica et Cosmochimica Acta 70, 1710-1727.

Tipper, E.T., Calmels, D., Gaillardet, J., Louvat, P., Capmas, F., Dubacq, B., 2012a. Positive correlation between Li and Mg isotope ratios in the river waters of the Mackenzie Basin challenges the interpretation of apparent isotopic fractionation during weathering. Earth and Planetary Science Letters 333–334, 35-45.

Tipper, E.T., Lemarchand, E., Hindshaw, R.S., Reynolds, B.C., Bourdon, B., 2012b. Seasonal sensitivity of weathering processes: Hints from magnesium isotopes in a glacial stream. Chemical Geology 312-313, 80-92.

1013 Tipper, E.T., Gaillardet, J., Louvat, P., Capmas, F., White, A.F., 2010. Mg isotope constraints on soil pore-fluid
1014 chemistry: Evidence from Santa Cruz, California. Geochimica et Cosmochimica Acta 74, 3883-3896.

1015 Tipper, E.T., Galy, A., Bickle, M.J., 2008. Calcium and magnesium isotope systematics in rivers draining the
1016 Himalaya-Tibetan-Plateau region: Lithological or fractionation control? Geochimica et Cosmochimica Acta 72,
1017 1057-1075.

1018 Tipper, E.T., Galy, A., Gaillardet, J., Bickle, M.J., Elderfield, H., Carder, E.A., 2006. The magnesium isotope
1019 budget of the modern ocean: Constrains from riverine magnesium isotope ratios. Earth and Planetary Science
1020 Letters 250, 241-253.

1021 Tishchenko, V., Meile, C., Scherer, M.M., Pasakarnis, T.S., Thompson, A., 2015. Fe^{2+} catalyzed iron atom
1022 exchange and re-crystallization in a tropical soil. Geochimica et Cosmochimica Acta 148, 191-202.

1023 Tomascak, P.B., Magna, T., Dohmen, R., 2016. Advances in Lithium Isotope Geochemistry. Springer
1024 International Publishing.

1025 Trostle, K., Derry, L., Vigier, N. and Chadwick, O., 2014. Magnesium Isotope Fractionation During Arid
1026 Pedogenesis on the Island of Hawaii (USA). Procedia Earth and Planetary Science 10, 243-248.

1027 Violante, A., Krishnamurti, G.S.R., Huang, P.M., 2002. Impact of organic substances on the formation and
1028 transformation of metal oxides in soil environments, in: Huang, P.M., Bollag, J.-M., Senesi, N. (Eds.),
1029 Interactions Between Soil Particles and Microorganism: Impact on the Terrestrial Ecosystem, Chichester,
1030 England.

1031 Vitousek, P.M., 1984. Litterfall, Nutrient Cycling, and Nutrient Limitation in Tropical Forests. Ecology 65,
1032 285-298.

1033 White, A.F., Buss, H.L., 2013. Natural Weathering Rates of Silicate Minerals, in: Drever, J.I. (Ed.), Surface and
1034 Ground Water, Weathering and Soils. Elsevier.

1035 White, A.F., Schulz, M.S., Stonestrom, D.A., Vivit, D.V., Fitzpatrick, J., Bullen, T.D., Maher, K., Blum, A.E.,
1036 2009. Chemical weathering of a marine terrace chronosequence, Santa Cruz, California. Part II: Solute profiles,
1037 gradients and the comparisons of contemporary and long-term weathering rates. Geochimica et Cosmochimica
1038 Acta 73, 2769-2803.

White, A.F., Blum, A.E., Schulz, M.S., Vivit, D.V., Stonestrom, D.A., Larsen, M., Murphy, S.F., Eberl, D., 1998. Chemical weathering in a tropical watershed, Luquillo Mountains, Puerto Rico: I. Long-term versus short-term weathering fluxes. Geochimica et Cosmochimica Acta 62, 209-226.

Williams, M.W., Brown, A.D., Melack, J.M., 1993. Geochemical and hydrologic controls on the composition of surface water in a high-elevation basin. Sierra Nevada, California. Limnology and Oceanography 38, 775-797.

Wimpenny, J., Colla, C.A., Yin, Q.Z., Rustad, J.R., Casey, W.H., 2014. Investigating the behaviour of Mg isotopes during the formation of clay minerals. Geochimica et Cosmochimica Acta 128, 178-194.

Wimpenny, J., Colla, C.A., Yu, P., Yin, Q.-Z., Rustad, J.R., Casey, W.H., 2015. Lithium isotope fractionation during uptake by gibbsite. Geochimica et Cosmochimica Acta 168, 133-150.

Wimpenny, J., Gíslason, S.R., James, R.H., Gannoun, A., Pogge Von Strandmann, P.A.E., Burton, K.W., 2010. The behaviour of Li and Mg isotopes during primary phase dissolution and secondary mineral formation in basalt. Geochimica et Cosmochimica Acta 74, 5259-5279.

Wohl, E., Barros, A., Brunsell, N., Chappell, N.A., Coe, M., Giambelluca, T., Goldsmith, S., Harmon, R., Hendrickx, J.M.H., Juvik, J., McDonnell, J., Ogden, F., 2012. The hydrology of the humid tropics. Nature Clim. Change 2, 655-662.

Wood, T.E., Lawrence, D., Clark, D.A., Chazdon, R.L., 2009. Rain forest nutrient cycling and productivity in response to large-scale litter manipulation. Ecology 90, 109-121.

Yi-Balan, S.A., Amundson, R., Buss, H.L., 2014. Decoupling of sulfur and nitrogen cycling due to biotic processes in a tropical rainforest. Geochimica et Cosmochimica Acta 142, 411-428.

Young, E.D., Galy, A., 2004. The isotope geochemistry and cosmochemistry of magnesium. Reviews in Mineralogy and Geochemistry 55, 197-230.

Figure captions

Figure 1. Location, general lithology and main watersheds of the Luquillo Critical Zone Observatory. Our field site is located over the volcaniclastic bedrock, in Bisley 1 watershed. The sampling sites used for this study are

depicted in the right-hand map. W1=bedrock drilling site; S1, S2, S3, S4=pore water sampling sites B1S1, B1S2, B1S3 and B1S4.

Figure 2. Concentration of Mg with depth in the ridgetop site (B1S1) in: a) pore water, b) exchangeable fraction (from Buss et al., 2017), and c) bulk regolith. All Mg concentration profiles generally increase with depth.

Figure 3. a) The fraction of parent rock Mg remaining in the weathered regolith of site B1S1 (f_{Mg}), as a function of depth, estimated using Nb as an immobile element (Eq. 2), shows a typical depletion profile from the bottom to 1.2 m depth. Above 1.2 m, Mg enrichment is evident towards the surface, although regolith Mg content is still ≤10% that of bedrock. b) Comparison of the degree of weathering in the different sites of this study, using the Weathering Index of Parker (WIP) as for Eq. (3). Fresh rocks should have WIP>100, whereas a completely weathered sample would have WIP=0. The ridgetop site (B1S1) is the most altered, whereas the valley site (B1S4) is the least.

Figure 4. Concentrations of Mg in pore water during 2008 in samples taken about every two months (open circles), and average value (closed circles). Mg that does not come from rain (Mg*), or 'rain-corrected', was estimated using the chlorine balance method as per White et al. (2009). Note that a similar graph appears in Chapela Lara et al. (2014), but Mg concentrations were given in the wrong units.

Figure 5. Pore water, exchangeable and bulk regolith δ^{26}Mg as a function of depth in the ridge top profile (B1S1). The error bar is 2sd from sea water δ^{26}Mg, as a measure of our overall uncertainty (− 0.07‰). Vegetation, rain and bedrock values are provided for reference (depth arbitrary). The shaded area represents the bedrock values±2sd.

Figure 6. Mg isotopic composition of pore water in profiles along the topo-sequence from ridge top to the riparian zone. Bedrock (B1W2-1-2), tabonuco bark, and rain are shown for reference (depth arbitrary). The slope transect covers an elevation gradient of ~18 m. Note the different scale in the X-axis for B1S1. The error bar is 2sd of seawater δ^{26}Mg (0.07‰). Modified from Chapela Lara et al. (2014).

Figure 7. Stage of water, Mg and δ^{26}Mg values in the Bisley 1 stream during a storm event. 2sd is about the size of the symbols. Modified from Chapela Lara et al. (2014).

Figure 8. Mg isotopic compositions of bedrock minerals analysed *in situ* by femtosecond laser ablation MC-ICP-MS on a thin section of sample B1W2-2-2. Error bars are 2SE. The horizontal line is the mean value of the bedrock samples analysed by solution MC-ICP-MS (open symbols), within the uncertainty of that method (shaded area). Bulk solution MC-ICP-MS analyses of samples B1W2-2-2 and B1W2-6-2 (open circle and square, respectively) are compared to fsLA-MC-ICP-MS analyses (closed circles and squares) of the same sample powders fused to a glass.

Figure 9. Magnesium isotope ratios of a) bulk regolith and b) the exchangeable fraction, compared to the abundance of Fe(III) minerals detected by XRD (goethite+hematite) and total iron contents (e); Mg contents in the exchangeable fraction compared with c) total iron and (d) Fe(III) minerals detected by XRD; f) number of bacterial cells vs. pore water δ^{26}Mg. All data are from the ridgetop site. The error bar represents the external uncertainty of δ^{26}Mg=0.07‰. [a] Values from Buss et al. (2017) and [b] Liermann et al. (2014).

Figure 10. Comparison of the stream samples and two fractionation models, using the average δ^{26}Mg of chlorite (+ 0.19‰) as the starting material. Several $\Delta_{i,s}$ values and deep pore water from site B1S1 (PW) are shown for comparison. a) Rayleigh fractionation model, the best fit to the data is for $\Delta_{i,s}$ between+ 0.50‰ and + 0.95‰ (Suppl. material). b) Steady state fractionation model, the separation factor ($\Delta_{i,s}$ = + 1.15‰) is obtained by solving Eq. (3). Error bars are our external error of 0.07‰ for the solution ICP-MS method for stream samples, and 2sd of chlorite measurements by laser ablation (Table 3).

Figure 11. Mg and δ^{26}Mg of all the water samples of this study. The blue arrow is the linear trend of the stream samples (r^2 = 0.98), pointing from baseflow to the peak of the storm. The [Mg] and δ^{26}Mg of pore water from each landscape unit was calculated using Eqs. 3 and S2 (Table 4). Horizontal lines represent the average δ^{26}Mg of chlorite, the bedrock and the rain. SSF = subsurface flow, the pore water flowing through the upper 20 cm of the regolith.

1123 **Figure 12**. Comparison of the degree of weathering of the regolith and the difference in $\delta^{26}Mg$ between the
1124 bedrock and streams, pore water and bulk regolith in silicate catchments. Samples from this work are depicted
1125 as closed symbols (pore water from site B1S1). CIA=100*(Al/(Al+Na+Ca+Mg)), with CIA=0 meaning a rock
1126 is not altered and CIA=100 meaning it is completely weathered. Mg isotope ratios are from Bolou-Bi et al.
1127 (2012), Dessert et al. (2015), Liu et al. (2014), Opfergelt et al. (2012), Teng et al. (2010) and Tipper et al.
1128 (2012b); only the minimum and maximum $\delta^{26}Mg$ values of the streams are given for each site. Where not given
1129 in the aforementioned references, the chemical alteration index is taken or calculated from Bernasconi et al.
1130 (2011), Clergue et al. (2015), and Henriet et al. (2008).
1131

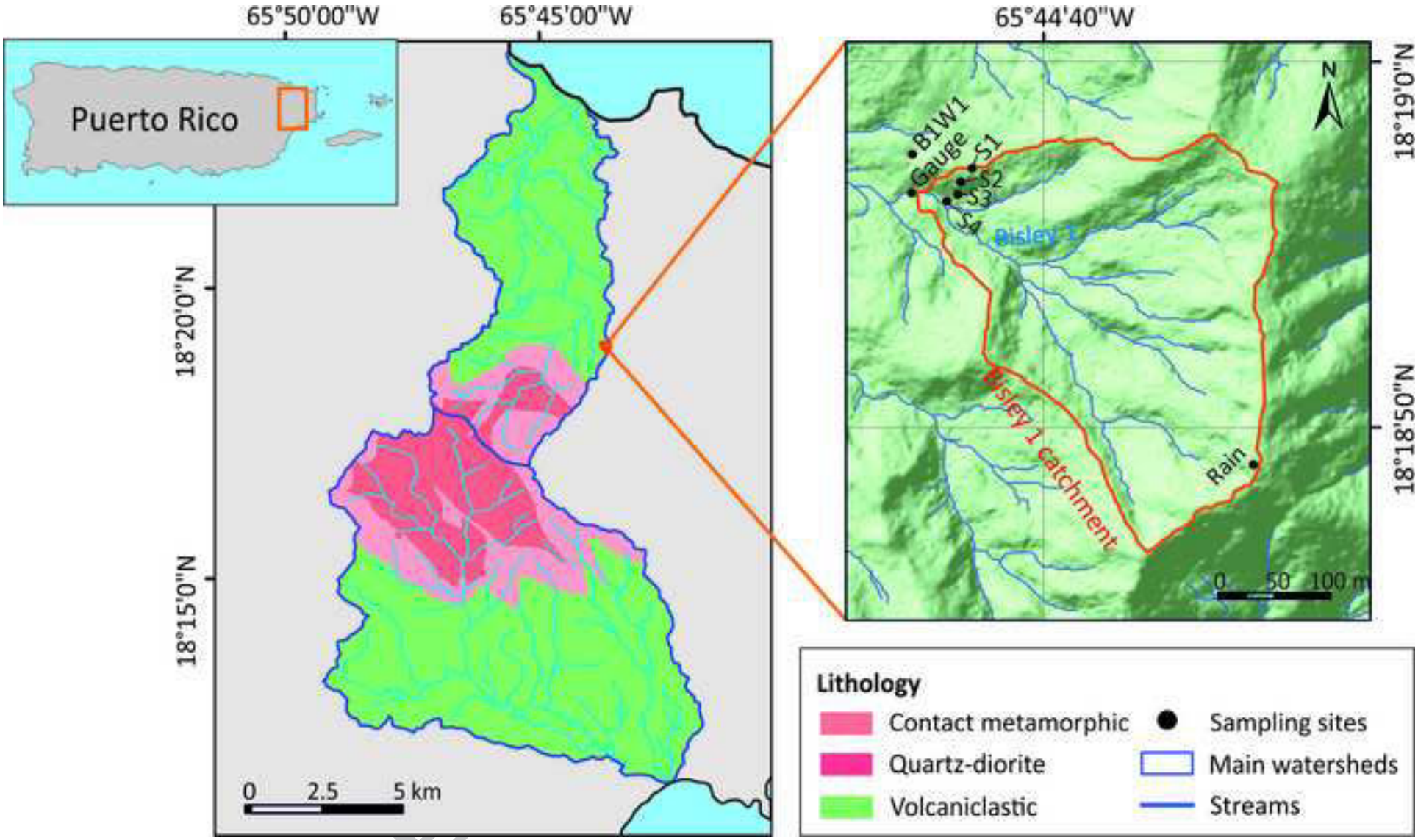

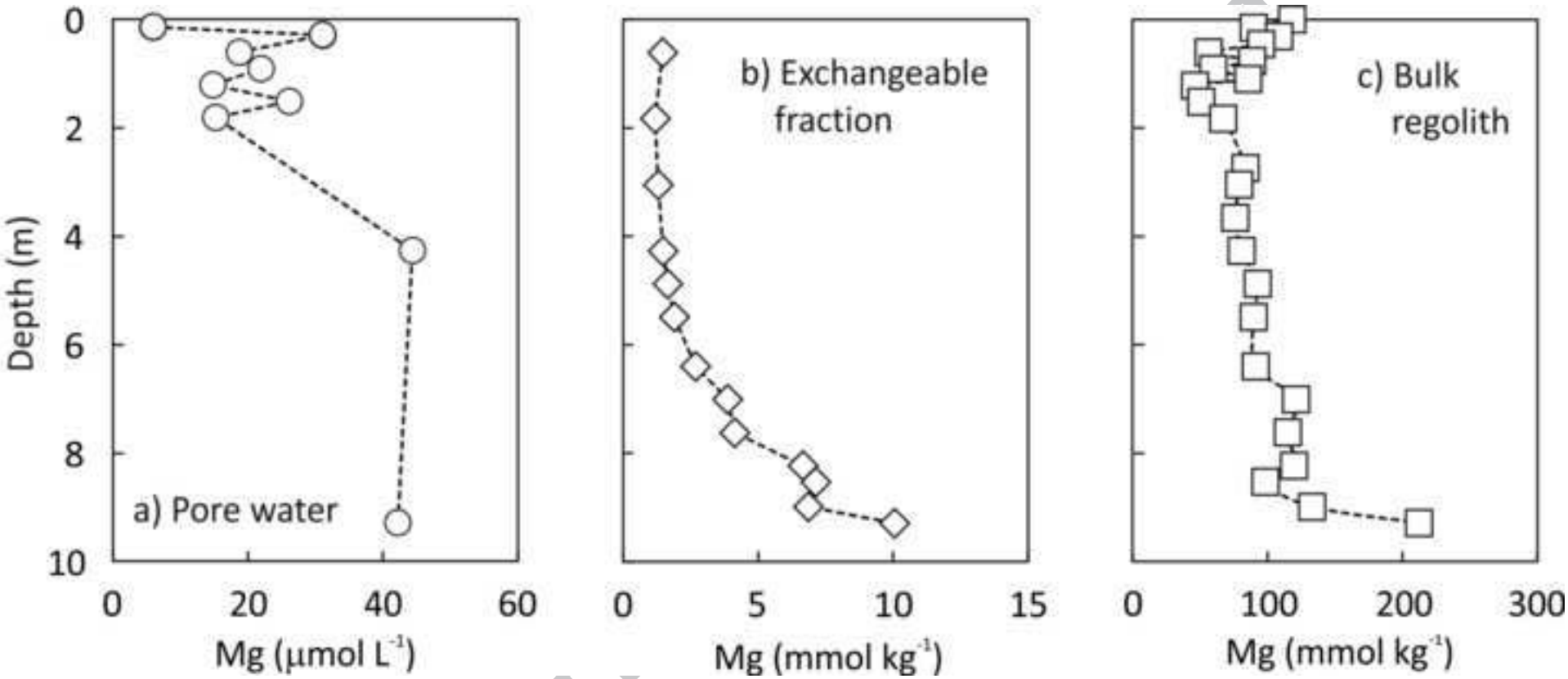

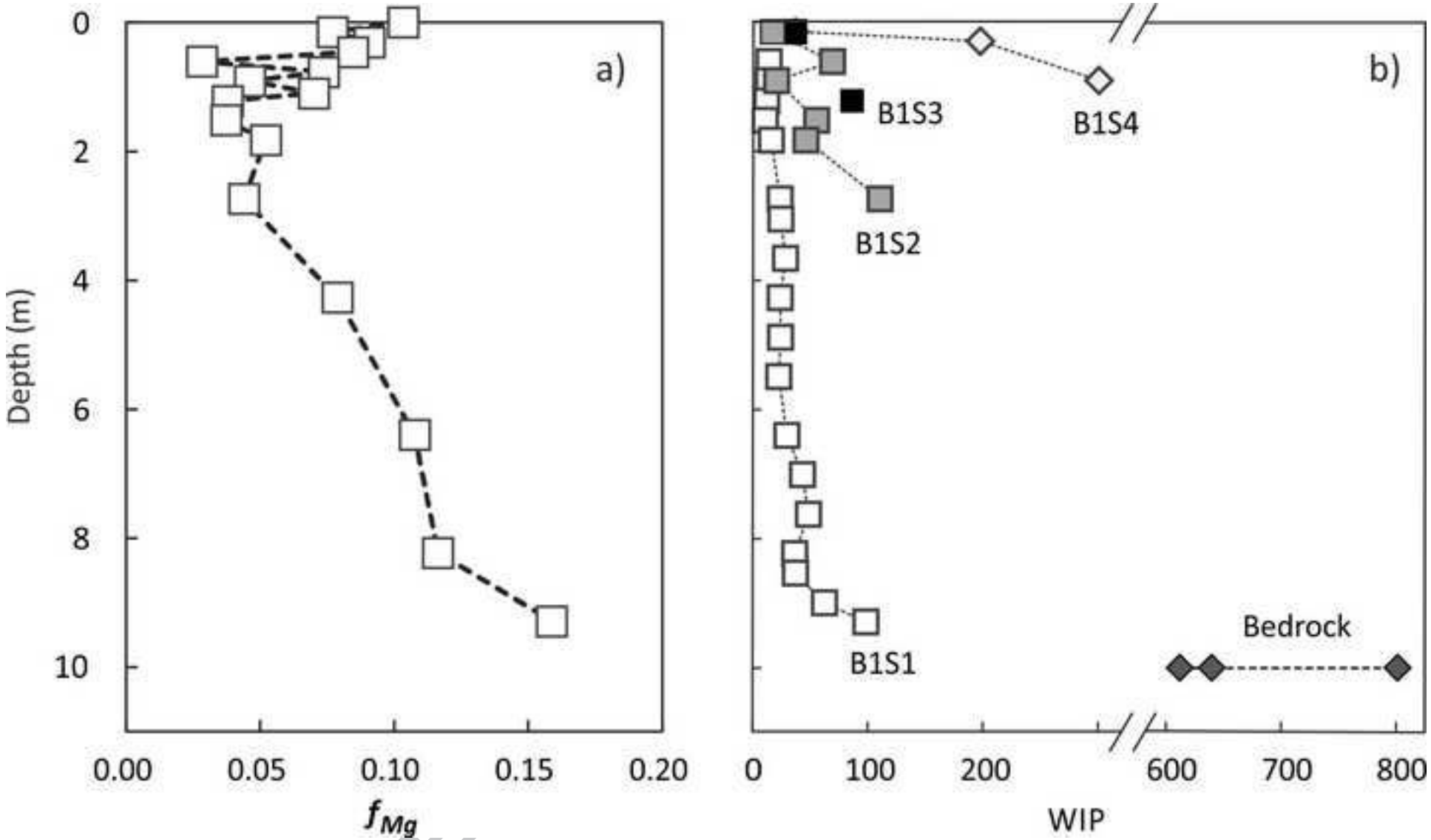

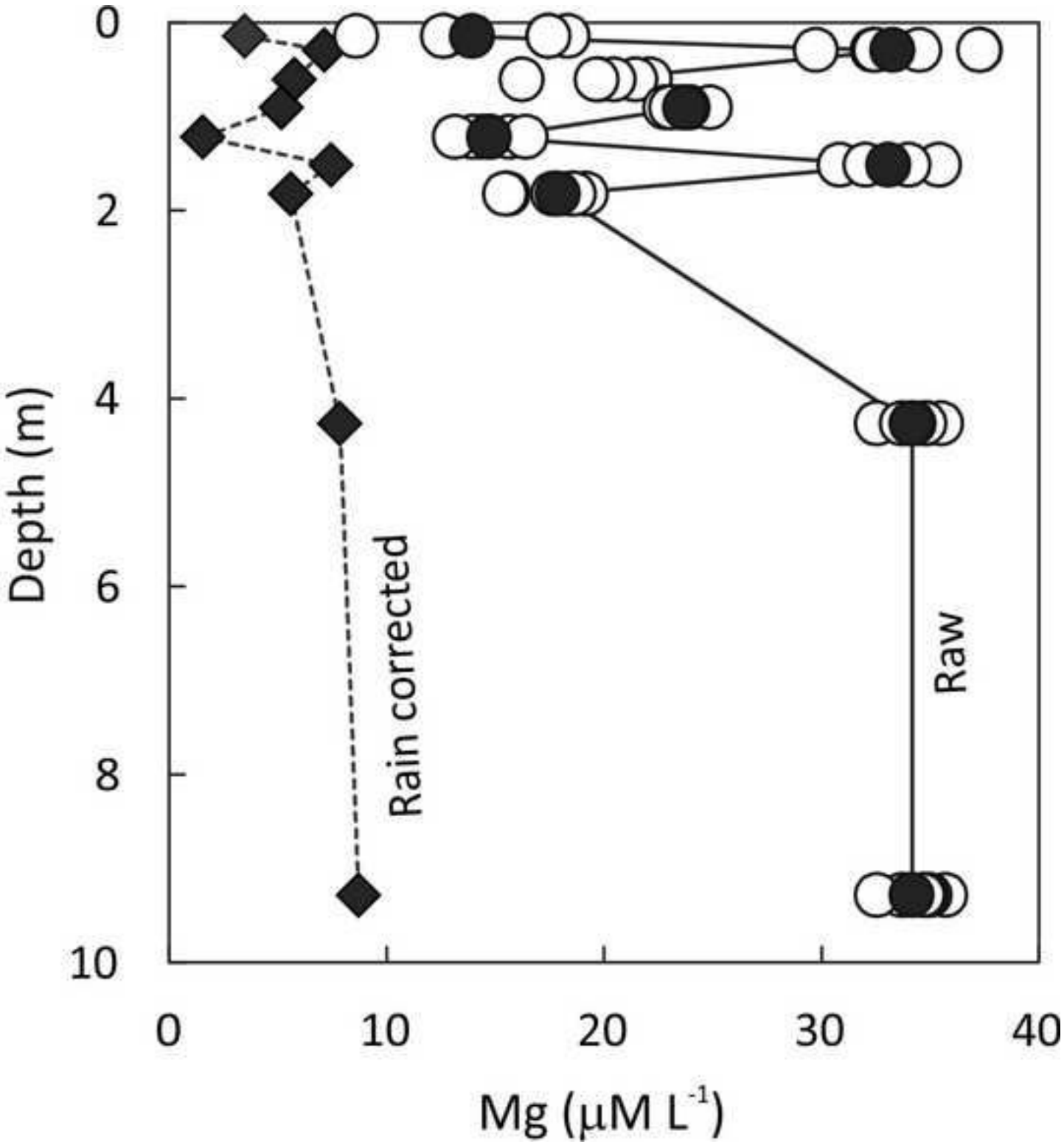

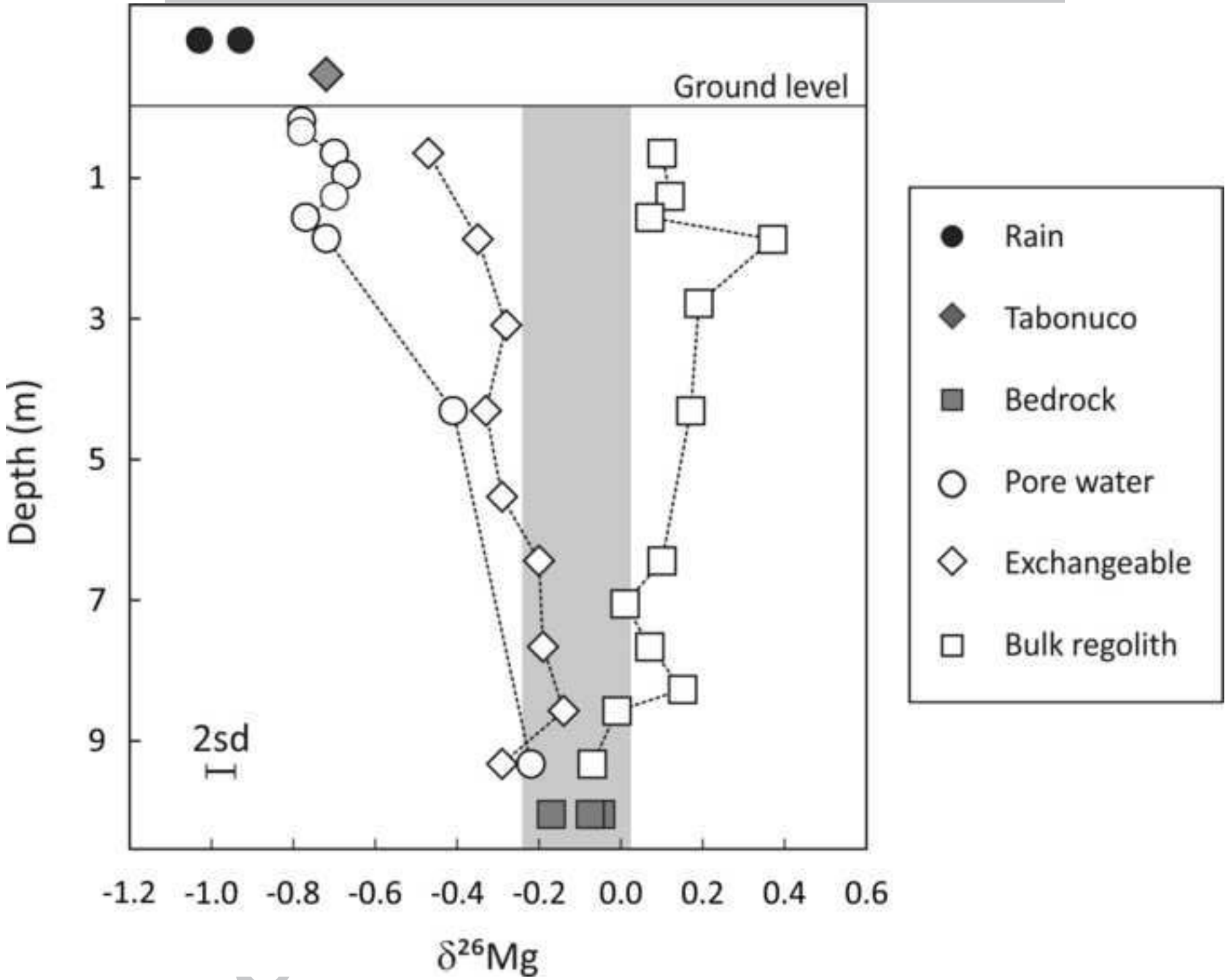

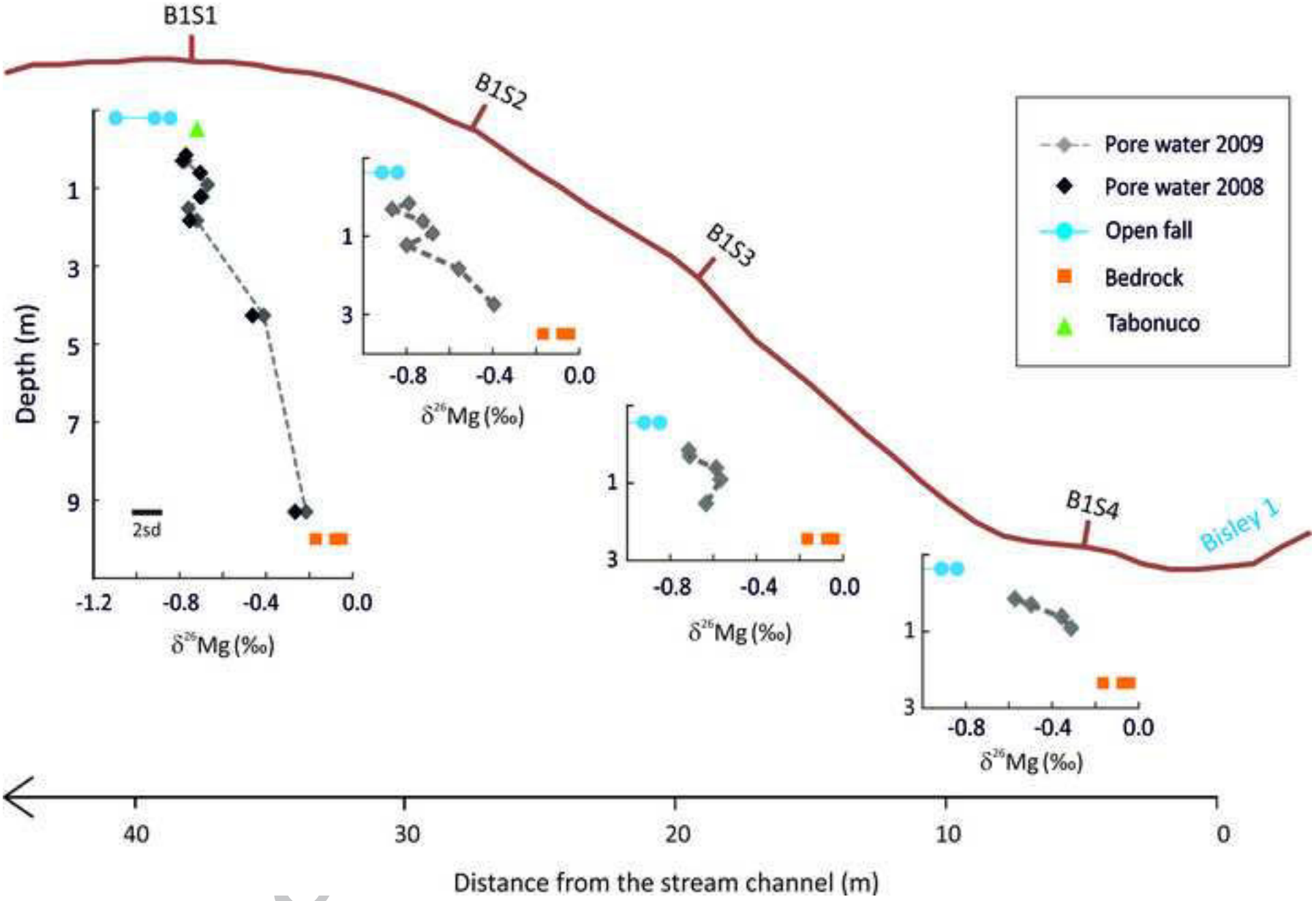

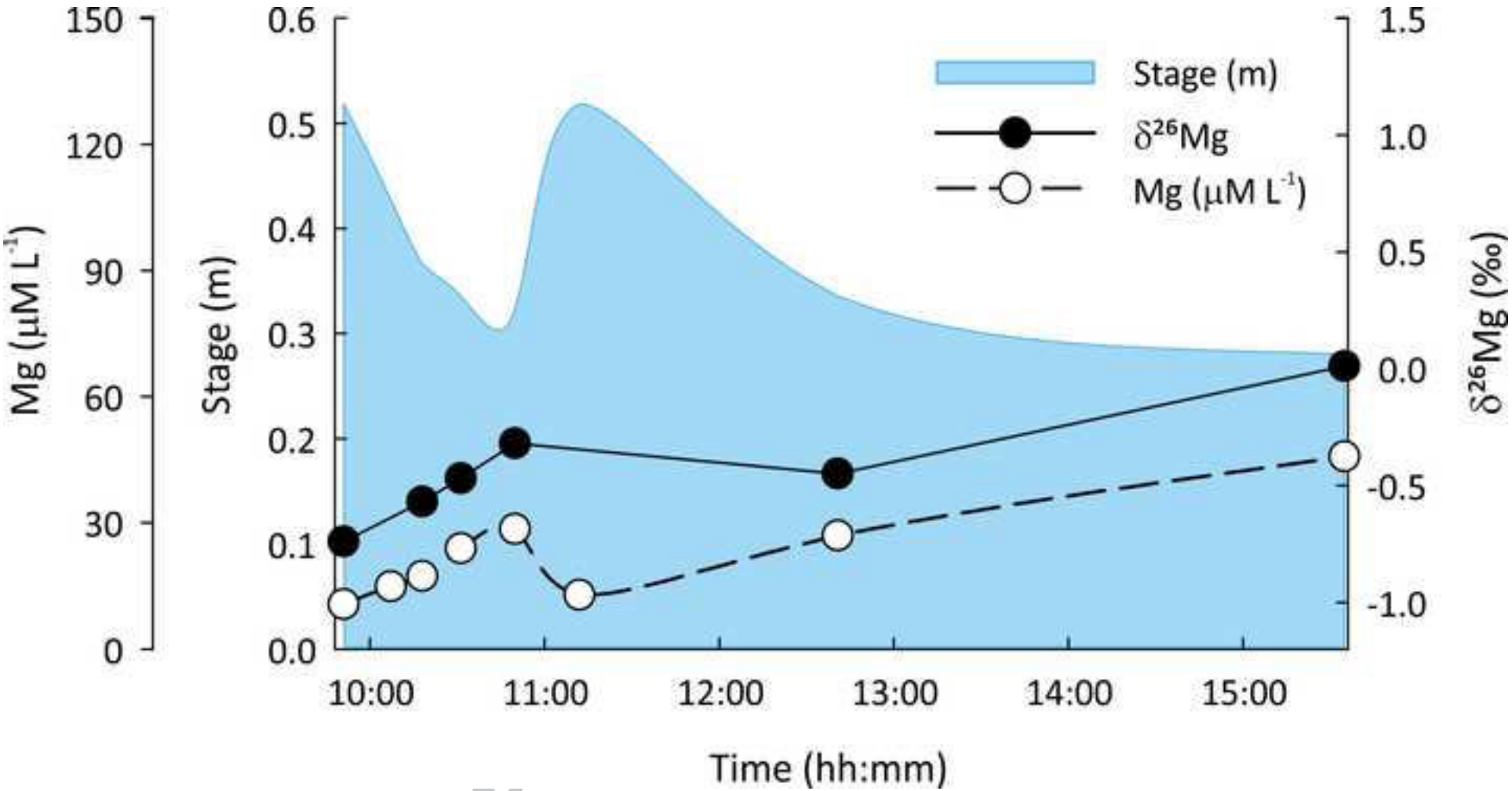

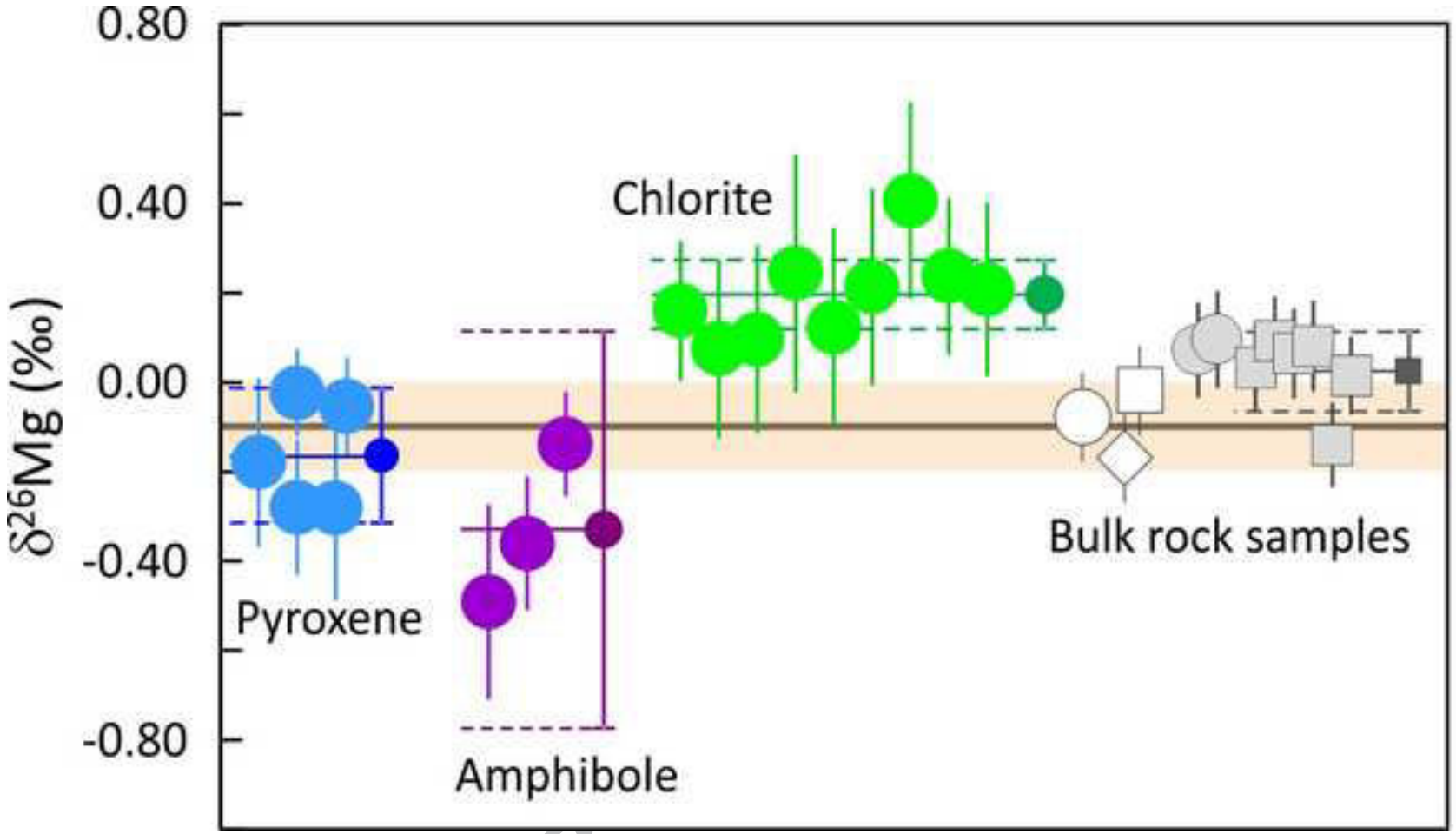

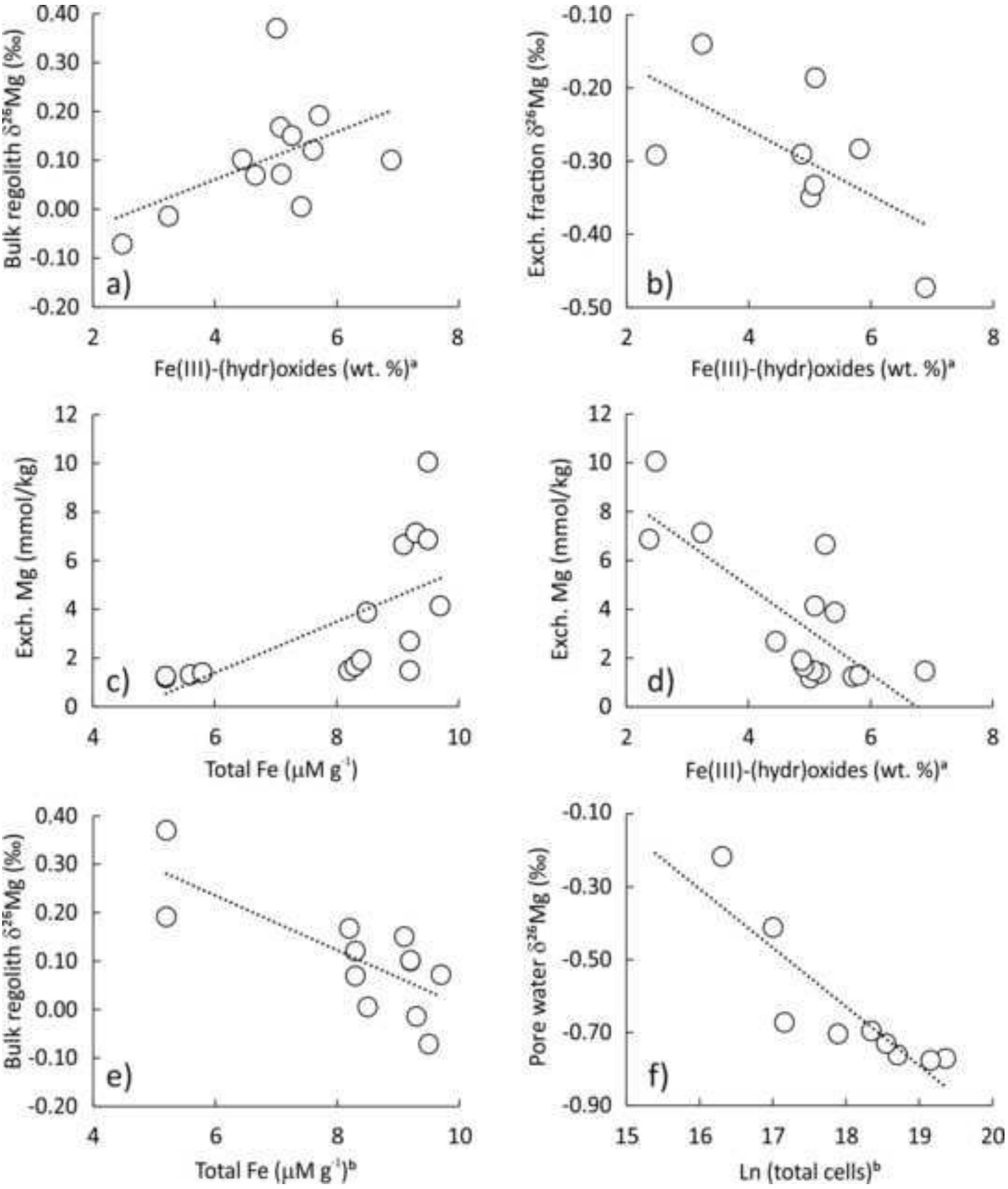

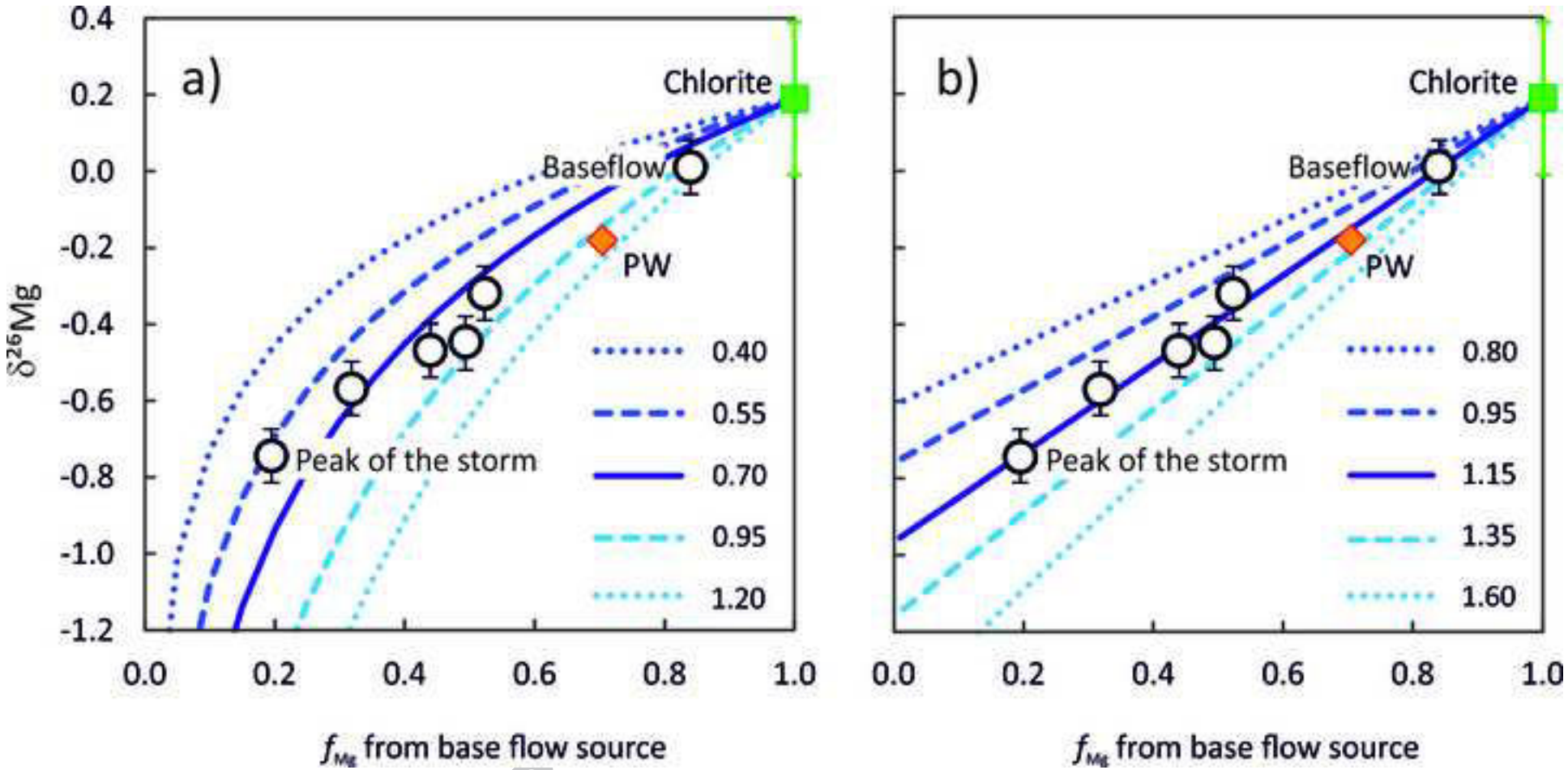

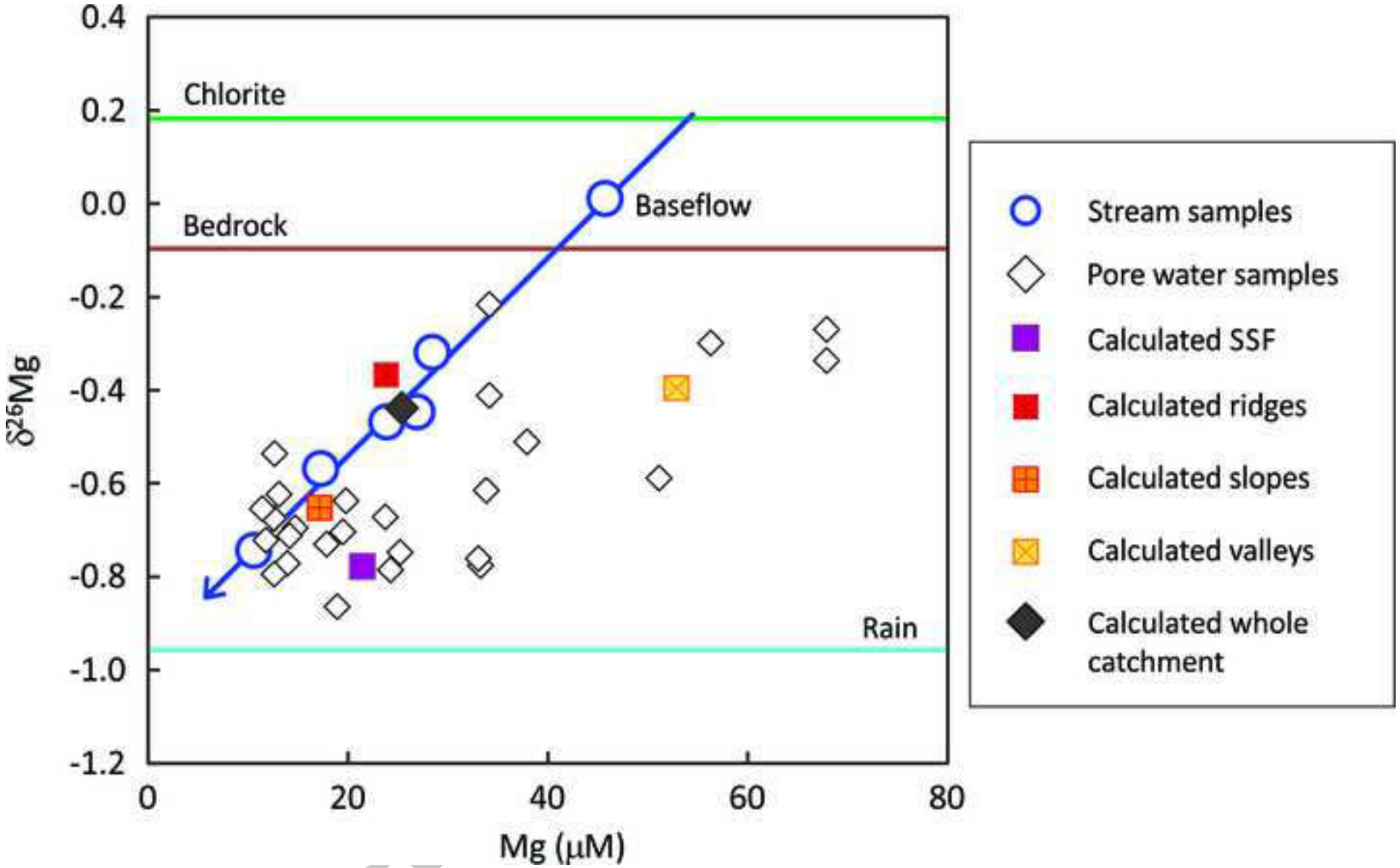

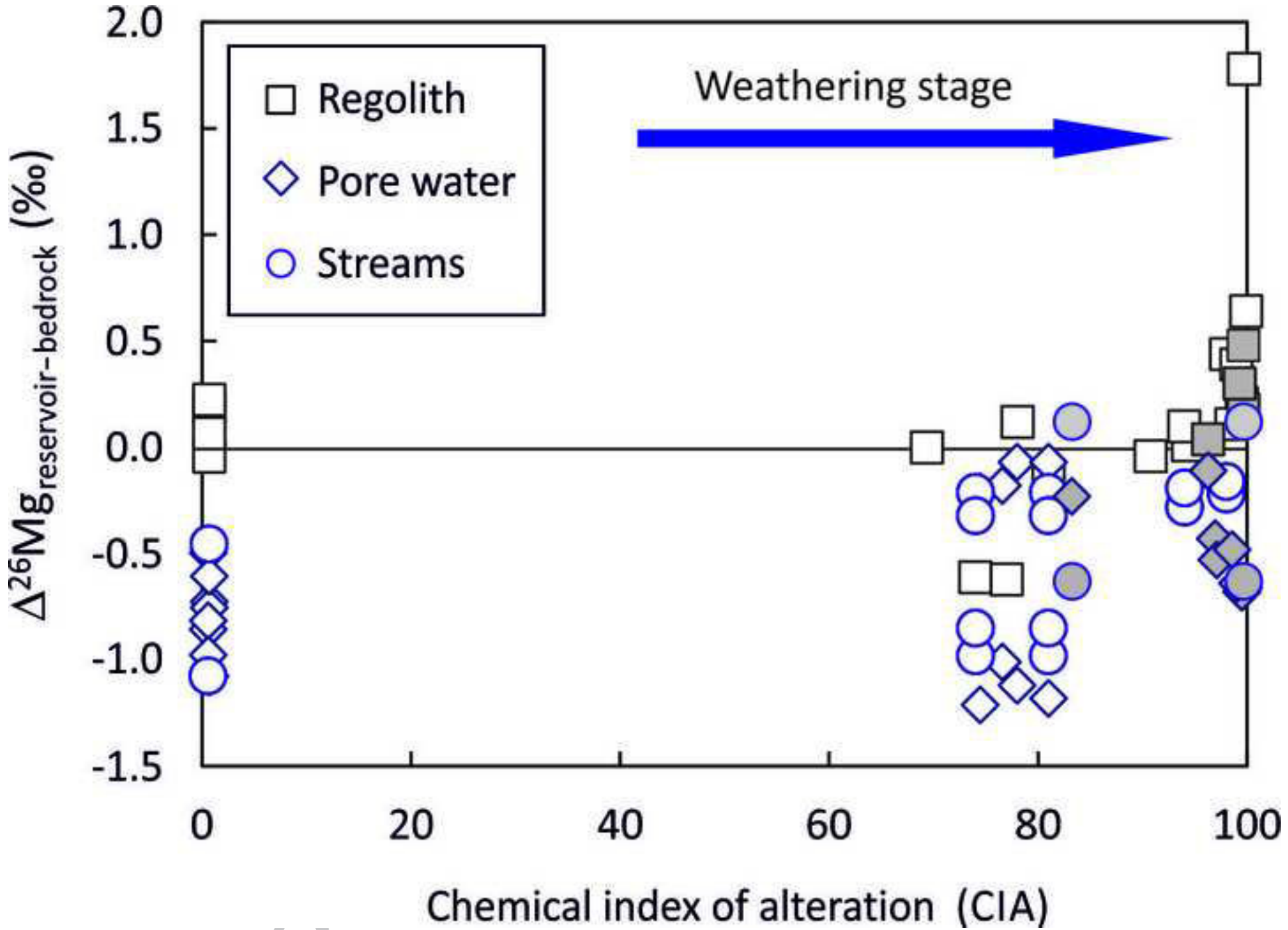

Tables

Table 1. General characteristics of the Bisley 1 catchment

Characteristic		Reference
Area	6.7 ha = 0.067 km^2	
Elevation [a]	261 to 410 masl	
Mean annual precipitation	3678±725 mm yr^{-1}	Gioda et al. (2013)
Mean daily temperature	24 ± 0.5 °C	Gioda et al. (2013)
Vegetation	Tabonuco forest (*Dacryodes excels*), sierra palm and ferns	Scatena (1989)
Soil type	Oxisols and Ultisols (US Soil Taxonomy); Ferralsols and Acrisols (WRB); 0.5 m to 1 m thick	Huffaker (2002)
Mineralogy (wt.%)[b]		
Regolith[c]	Disordered kaolinite: 30-82 wt%, microcrystalline Qz: 12-29 wt%, halloysite: 9-24 wt%; illite: 7-12 wt%; oxides: 2.5-9 wt% (goethite > gibbsite > hematite); minor Amp, Px, and Plg.	Buss and White (2012); Dosseto et al. (2012); Porder et al. (2015)
Regolith/bedrock transition	K-spar ~ 3%, Mg-rich chlorite ~ 10%	Buss and White (2012)
Bedrock	Plg = 36%, Chl = 23%, Qz =10%, Px = 9%, Amp = 4%, epidote = 8%, K-spar = 6%, prehnite = 2%, Bt <1%, illite = 1%, kaolinite < 1%	Buss et al. (2013, 2017)
Bedrock weathering rate	334 mm ky^{-1}	Dosseto et al. (2012)

[a] masl=meters above sea level.
[b] Plg = plagioclase, Qz = quartz, Chl = chlorite, Px = pyroxene, Amp = amphibole, K-spar = potassic feldspar, Bt = biotite.
[c] Including soil and saprolite.

1142 Table 2. Mg and δ^{26}Mg values of samples and standards analysed for this study

Sample	Depth	Mg	δ^{25}Mg	2SE	δ^{26}Mg	2SE	Δ^{25}Mg'	n
Units	m	µM L^{-1}	‰	‰	‰	‰	‰	
Pore-water								
B1S1-0.5	0.15	6.0	-0.40	0.01	-0.77	0.03	0.00	3
B1S1-0.5*	0.15		-0.45	0.03	-0.78	0.01	-0.05	2
B1S1-1	0.30	31.1	-0.41	0.01	-0.78	0.00	0.00	2
B1S1-2	0.61	18.8	-0.37	0.03	-0.68	0.02	-0.01	3
B1S1-2*	0.61		-0.40	0.01	-0.70	0.03	-0.04	3
B1S1-3	0.91	22.0	-0.36	0.02	-0.67	0.02	-0.01	3
B1S1-4	1.22	14.8	-0.36	0.00	-0.70	0.01	0.00	2
B1S1-4*	1.22		-0.36	0.02	-0.68	0.02	0.00	3
B1S1-5	1.52	26.2	-0.38	0.00	-0.76	0.00	0.01	2
B1S1-5*	1.52		-0.40	0.01	-0.77	0.01	-0.02	2
B1S1-6	1.82	15.3	-0.35	0.01	-0.73	0.03	0.01	2
B1S1-6*	1.82		-0.41	0.02	-0.72	0.01	-0.03	4
B1S1-14	4.27	44.4	-0.24	0.02	-0.41	0.00	-0.02	2
B1S1-30.5	9.30	42.3	-0.12	0.02	-0.22	0.01	0.01	3
B1S2-0.5	0.15	26.2	-0.40	0.02	-0.79	0.02	0.01	3
B1S2-1	0.30	25.0	-0.45	0.02	-0.86	0.00	0.00	3
B1S2-2	0.61	11.6	-0.39	0.02	-0.72	0.02	-0.02	2
B1S2-3	0.91	14.8	-0.38	0.01	-0.68	0.01	-0.03	2
B1S2-3*	0.91		-0.38	0.01	-0.71	0.00	-0.01	3
B1S2-4	1.22	13.4	-0.46	0.01	-0.80	0.01	-0.04	2
B1S2-6	1.83	13.9	-0.34	0.03	-0.62	0.01	-0.01	3
B1S2-6*	1.83		-0.27	0.02	-0.55	0.01	0.02	3
B1S2-9	2.74	13.3	-0.30	0.02	-0.54	0.01	-0.02	3
B1S3-0.5	0.15	25.3	-0.41	0.01	-0.75	0.01	-0.03	3
B1S3-0.5*	0.15		-0.40	0.03	-0.72	0.01	0.00	2
B1S3-0.5**	0.15		-0.41	0.04	-0.79	0.00	-0.01	2
B1S3-1	0.30	14.2	-0.41	0.00	-0.74	0.00	-0.03	1
B1S3-1*	0.30		-0.40	0.01	-0.71	0.00	-0.03	2
B1S3-2	0.61	11.5	-0.37	0.01	-0.65	0.04	-0.01	2
B1S3-3	0.91	33.9	-0.34	0.02	-0.61	0.01	0.01	3
B1S3-3*	0.91		-0.29	0.01	-0.57	0.00	-0.03	2
B1S3-5	1.52	19.8	-0.36	0.02	-0.64	0.01	-0.02	3
B1S3-5*	1.52		-0.33	0.05	-0.58	0.00	-0.03	3
B1S4-0.5	0.15	51.2	-0.33	0.04	-0.59	0.02	-0.03	3
B1S4-0.5*	0.15		-0.31	0.00	-0.59	0.00	-0.01	1
B1S4-1	0.30	37.9	-0.27	0.03	-0.51	0.03	-0.01	3
B1S4-1*	0.30		-0.27	0.02	-0.52	0.01	0.00	3
B1S4-1**	0.30		-0.30	0.01	-0.51	0.01	-0.04	3
B1S4-2	0.61	56.3	-0.24	0.01	-0.38	0.02	-0.04	2
B1S4-3	0.91	67.9	-0.20	0.02	-0.34	0.07	-0.03	2

Rain (openfall)								
BOF			-0.57	0.00	-1.10	0.05	0.00	2
LQR3			-0.51	0.03	-0.93	0.02	-0.03	2
LQR3*			-0.49	0.03	-0.92	0.02	-0.01	2
Exchangeable fraction								
		mmol kg^{-1}						
B1S1 61	0.61	1.47	-0.25	0.03	-0.47	0.03	-0.01	3
B1S1 61*	0.61		-0.24	0.03	-0.42	0.04	0.00	3
B1S1 183	1.83	1.19	-0.19	0.02	-0.35	0.02	-0.01	2
B1S1 183*	1.83		-0.17	0.03	-0.27	0.02	-0.01	2
B1S1 305	3.05		-0.21	0.03	-0.28	0.02	-0.06	3
B1S1 427	4.27		-0.21	0.01	-0.33	0.02	-0.04	3
B1S1 549	5.49	1.91	-0.16	0.06	-0.29	0.01	-0.01	2
B1S1 640	6.40	2.69	-0.09	0.04	-0.20	0.04	0.01	2
B1S1 640*	6.40		-0.07	0.08	-0.13	0.05	0.00	2
B1S1 762	7.62	4.13	-0.10	0.01	-0.19	0.03	0.00	3
B1S1 853	8.53	7.13	-0.02	0.05	-0.08	0.03	0.02	3
B1S1 853*	8.53		-0.08	0.02	-0.14	0.01	0.00	2
B1S1 929	9.29	10.06	-0.16	0.02	-0.29	0.01	-0.01	3
Bulk regolith								
		MgO wt.%						
B1-061	0.61	0.29	0.04	0.01	0.10	0.02	-0.01	3
B1-091	0.91	0.29						
B1-122	1.22	0.23	0.06	0.01	0.12	0.05	-0.01	2
B1-152	1.52	0.24	0.03	0.01	0.07	0.00	-0.01	3
B1-183	1.83	0.45	0.21	0.03	0.37	0.02	0.02	2
B1-274	2.74	0.48	0.11	0.05	0.19	0.02	0.01	2
B1-305	3.05	0.53						
B1-366	3.66	0.51						
B1-427	4.27	0.54	0.09	0.04	0.17	0.04	0.00	2
B1-488	4.88	0.62						
B1-549	5.49	0.60						
B1-640	6.40	0.61	0.04	0.03	0.10	0.03	-0.01	2
B1-701	7.01	0.81	-0.01	0.10	0.01	0.02	-0.01	2
B1-762	7.62	0.77	0.03	0.05	0.07	0.04	0.00	2
B1-823	8.23	0.80	0.07	0.05	0.15	0.02	-0.01	2
B1-853	8.53	0.66	-0.01	0.04	-0.01	0.03	0.00	2
B1-929	9.29	1.42	-0.02	0.04	-0.07	0.03	0.02	2
Drilled bedrock								
B1W2-1-2	4.4	5.8	-0.09	0.01	-0.17	0.01	0.00	3
B1W2-2-2	6.4	5.0	-0.05	0.02	-0.08	0.04	-0.02	4
B1W2-6-2	12.0	5.2	0.00	0.04	-0.05	0.03	0.02	3

Tabonuco bark	0.5	-0.42	0.00	-0.72	0.04	-0.05	2

Stream water during a storm event

	Time	**Stage**	**Mg**	**δ^{25}Mg**	**2SE**	**δ^{26}Mg**	**2SE**	**Δ^{25}Mg'**	**n**
	hh:mm	m	µM L^{-1}	‰	‰	‰	‰	‰	
StrB62	09:51	0.52	10.63	-0.43	0.02	-0.74	0.03	-0.04	3
StrB63	10:07	0.43	14.89						
StrB64	10:18	0.37	17.34	-0.30	0.03	-0.57	0.02	0.00	2
StrB65	10:31	0.34	23.93	-0.24	0.01	-0.47	0.01	0.01	2
StrB65*	10:31	0.34	23.93	-0.24	0.00	-0.44	0.01	-0.01	3
StrB66	10:50	0.32	28.50	-0.18	0.03	-0.32	0.02	-0.02	3
StrB67	11:12	0.52	12.86						
StrB68	12:41	0.34	26.94	-0.25	0.02	-0.45	0.02	-0.02	3
StrB61	15:35	0.28	45.76	0.01	0.02	0.01	0.03	0.00	3

Reference Materials

	δ^{25}Mg	**2SE**	**δ^{26}Mg**	**2SE**	**Δ^{25}Mg'**	**n**
	‰	‰	‰	‰	‰	
Soil pore water (B1S1)	-0.41	0.01	-0.77	0.01	-0.01	14
CAM-1	-1.32	0.01	-2.56	0.01	0.01	54
Seawater	-0.45	0.02	-0.85	0.02	-0.01	13
BCR-2	-0.17	0.04	-0.29	0.08	-0.02	3
BHVO-2	-0.10	0.01	-0.20	0.03	0.00	2

*Duplicate. **Triplicate.

2SE = two times the standard error; n = number of measurements by ICP-MS.

Δ^{25}Mg' is the deviation from the predicted equilibrium mass-dependent fractionation law (slope = 0.521; Young and Galy, 2004).

1143

Table 3. Mg isotopes[a], and Mg and Al concentration[b] analyses by fsLA-MC-ICP-MS

Analysis ID	Material type	$\delta^{26}Mg_{DSM-3}$ ‰	2SE	$\delta^{25}Mg_{DSM-3}$ ‰	2SE	Si (*IS*) wt%	Al wt%	2SE	Mg wt%	2SE
Sample B1W2-2-2 - single mineral grains analysed by fsLA-MC-ICP-MS										
P1	Pyroxene	-0.18	0.19	-0.04	0.11	24.20	1.02	0.02	9.13	0.11
P8	Pyroxene	-0.28	0.15	-0.17	0.09	24.20	1.76	0.04	9.89	0.13
P9	Pyroxene	-0.28	0.21	-0.21	0.12	24.20	1.05	0.03	8.40	0.11
P16	Pyroxene	-0.05	0.11	-0.03	0.07	24.20	1.15	0.02	10.46	0.13
P17	Pyroxene	-0.02	0.10	0.03	0.07	24.20	1.13	0.03	8.75	0.11
	mean	**-0.16**		**-0.09**			**1.22**		**9.33**	
	2SD (n=5)	**0.24**		**0.20**			**0.61**		**1.69**	
P14	Amphibole[c]	-0.49	0.22	-0.31	0.14	25.29	2.36	0.06	9.89	0.16
Chl1	Amphibole[c]	-0.36	0.15	-0.19	0.10	25.29	2.92	0.10	9.14	0.14
P18	Amphibole[c]	-0.14	0.12	-0.07	0.07	25.29	3.83	0.11	7.32	0.11
	mean	**-0.33**		**-0.19**			**3.04**		**8.78**	
	2SD (n=3)	**0.36**		**0.25**			**1.49**		**2.64**	
Chl4	Chlorite	0.16	0.16	0.08	0.09	13.74	9.73	0.21	9.73	0.24
Chl7	Chlorite	0.07	0.20	0.08	0.12	13.74	7.71	0.18	6.42	0.16
C10	Chlorite	0.10	0.21	0.08	0.12	13.74	9.94	0.21	11.53	0.24
C11	Chlorite	0.24	0.27	0.09	0.15	13.74	7.53	0.19	7.45	0.16
C12	Chlorite	0.12	0.22	0.11	0.13	13.74	9.10	0.22	9.29	0.16
C14	Chlorite	0.21	0.22	0.08	0.12	13.74	9.80	0.22	10.64	0.17
C15	Chlorite	0.40	0.22	0.22	0.13	13.74	9.82	0.22	10.25	0.16
C16	Chlorite	0.24	0.17	0.09	0.11	13.74	9.47	0.21	10.75	0.17
C17	Chlorite	0.21	0.19	0.08	0.11	13.74	9.47	0.20	10.95	0.15
	mean	**0.19**		**0.10**			**9.18**		**9.67**	
	2SD (n=9)	**0.20**		**0.09**			**1.84**		**3.40**	

Sample powder fused to glass by Ir strip heater and analysed by fsLA-MC-ICP-MS								
B1W2-2-2	mean	0.08	0.06	24.50	8.91		3.05	24.50
	2SD (n=2)	0.03	0.03		0.09		0.03	
B1W2-6-2	mean	0.02	0.01	24.50	8.56		3.06	24.50
	2SD (n=6)	0.17	0.16		0.10		0.04	
Reference values from bulk solution MC-ICP-MS (Table 2)				*Concentration reference values (Table S1)*				
B1W2-2-2	mean	-0.08	-0.05	24.68	9.00		3.03	
	2SD (n=4)	0.02	0.06	1.23	0.45		0.15	
B1W2-6-2	mean	-0.05	0.00	25.25	8.90		3.15	
	2SD (n=3)	0.05	0.06	1.26	0.45		0.16	
BHVO-2G basalt glass reference material analysed by fsLA-MC-ICP-MS								
	mean	-0.17	-0.10	23.05	7.05		4.28	
	2SD (n=26)	0.25	0.12		0.36		0.15	
BHVO-2 reference values (published)								
	mean	-0.22	-0.11	23.05	7.20	0.05	4.30	0.01
	2SD	0.09	0.06					

[a] Analysis by Neptune MC-ICP-MS (wet plasma, Jet+X-cone, high-resolution mode) coupled to fsLA: line scan with 25 µm laser spot (1 J/cm²), bracketing with MPI DING GOR132-G (presented data recalculated to DSM-3 scale).
2SE is the internal counting statistical uncertainty of individual analysis. However, repeat analyses of BHVO-2G and comparison to the published reference values indicate an uncertainty estimate of better than 0.25‰ (2SD) for δ^{26}Mg and 0.12‰ (2SD) for δ^{25}Mg of the laser ablation data.
[b] ^{27}Al and ^{28}Si signals measured simultaneously with Mg isotopes during laser ablation; calibration for concentrations via GOR132-G using ^{28}Si as internal standard *(IS)*.
Repeat analyses of BHVO-2G and comparison to the published reference values indicate a relative uncertainty estimate of better than 5% (2RSD) for Al and Mg concentrations.
[c] Amphiboles were highly altered and therefore the laser ablation analyses do not represent pure amphibole, also indicated by the higher grain-to-grain variability.

1
2 Table 4. Calculation of stream water [Mg] and δ^{26}Mg based on different flow paths

	Area	**Area**	**Depth***	f_{Mg}	**Mg**	**δ^{26}Mg**
	ha	fraction	m		µmol L^{-1}	‰
	Subsurface shallow flow water (SSF)					
Ridges	0.15	0.23	0.2	0.11	13.9	– 0.77
Slopes	0.37	0.55	0.2	0.47	24.3	– 0.79
Valleys	0.15	0.22	0.2	0.42	52.5	– 0.59
		Calculated pore water composition:			**34.8**	**– 0.70**
	Whole regolith pore water					
Ridges	0.15	0.23	16.0	0.65	23.9	– 0.37
Slopes	0.37	0.55	3.0	0.24	17.2	– 0.67
Valleys	0.15	0.22	1.0	0.11	56.2	– 0.40
		Calculated pore water composition:			**30.4**	**– 0.44**

Water content set constant to 28%.
Full calculation procedure in the supplementary material, page 2.
* Area under a concentration vs. depth curve.

3
4

5 Table 5. Pools, fluxes, and isotopic composition of Mg into, out of, and within the Bisley 1 catchment

	Mg	**δ^{26}Mg (‰)**
Fluxes	(kg ha^{-1} yr^{-1})	
Rainfall	13 [a]	– 0.92 to – 1.10
Litterfall	16 [b], 19 [c]	
Saharan dust	3 [d]	– 0.22
Bedrock dissolution	35 [e]	– 0.10
Chlorite dissolution	19 [f]	+ 0.19
Stream dissolved load	51 [a]	– 0.57 to + 0.01
Pools	(kg ha^{-1})	
Vegetation	192 [g]	– 0.72
Pore water	32 to 57 [h]	– 0.86 to – 0.14
Regolith exchangeable fraction	13690 [i]	– 0.47 to – 0.08
Bulk regolith	150455 [i]	– 0.07 to + 0.37

[a] Our calculations, from LTER database long-term averages (Table S5).
[b] McDowell and Asbury (1994).
[c] Porder et al. (2015), calculated from Ostertag et al. (2003).
[d] Our calculations, from dust flux in Pett-Ridge et al. (2009) and [Mg] in dust in Reid et al. (2003); δ^{26}Mg is the average weighted value of the upper continental crust (Li et al., 2010).
[e] From the catchment mass balance (Eq. 4); δ^{26}Mg is the average value of measured

bedrock samples (Table 2).

[f] From the catchment mass balance (Eq. 4), and the abundance of chlorite in the bedrock (Buss et al., 2013); δ^{26}Mg is the average value of measured chlorite (Table 3).

[g] Scatena et al. (1993) from forest plots similar to ours but not exactly in the same location.

[h] Our calculations, from landscape areas in Table 4, [Mg] in Table S5, and water content averaged from Buss et al. (2017) and Liermann et al. (2014).

[i] Our calculations, using the regolith bulk density from Buss et al. (2017).

6
7
8